



Contents lists available at ScienceDirect

## International Journal of Heat and Mass Transfer

journal homepage: [www.elsevier.com/locate/ijhmt](http://www.elsevier.com/locate/ijhmt)

# Experimental investigation of frequency and amplitude of density wave oscillations in vertical upflow boiling



Lucas E. O'Neill<sup>a</sup>, Issam Mudawar<sup>a,\*</sup>, Mohammad M. Hasan<sup>b</sup>, Henry K. Nagra<sup>b</sup>, R. Balasubramanian<sup>b</sup>, Jeffery R. Mackey<sup>c</sup>

<sup>a</sup> Purdue University Boiling and Two-Phase Flow Laboratory (PU-BTPFL), School of Mechanical Engineering, Purdue University, 585 Purdue Mall, West Lafayette, IN 47907, USA

<sup>b</sup> NASA Glenn Research Center, 21000 Brookpark Road, Cleveland, OH 44135 USA

<sup>c</sup> Vantage Partners, 3000 Aerospace Parkway, Brook Park, OH 44142, USA

## ARTICLE INFO

### Article history:

Received 28 November 2017

Received in revised form 25 April 2018

Accepted 26 April 2018

Available online 16 May 2018

### Keywords:

Flow boiling

Flow instabilities

Density wave oscillations

Frequency and amplitude

## ABSTRACT

Historically, study of two-phase flow instabilities has been arguably one of the most challenging endeavors in heat transfer literature due to the wide range of instabilities systems can manifest depending on differences in operating conditions and flow geometry. This study utilizes experimental results for vertical upflow boiling of FC-72 in a rectangular channel with finite inlet quality to investigate Density Wave Oscillations (DWOs) and assess their potential impact on design of two-phase systems for future space missions. High-speed flow visualization image sequences are presented and used to directly relate the cyclical passage of High and Low Density Fronts (HDFs and LDFs) to dominant low-frequency oscillations present in transient pressure signals commonly attributed to DWOs. A methodology is presented to determine frequency and amplitude of DWO induced pressure oscillations, which are then plotted for a wide range of relevant operating conditions. Mass velocity (flow inertia) is seen to be the dominant parameter influencing frequency and amplitude of DWOs. Amplitude of pressure oscillations is at most 7% of the time-averaged pressure level for current operating conditions, meaning there is little risk to space missions. Reconstruction of experimental pressure signals using a waveform defined by frequency and amplitude of DWO induced pressure fluctuations is seen to have only moderate agreement with the original signal due to the oversimplifications of treating DWO induced fluctuations as perfectly sinusoidal in nature, assuming they occur at a constant frequency value, and neglecting other transient flow features. This approach is nonetheless determined to have potential value for use as a boundary condition to introduce DWOs in two-phase flow simulations should a model be capable of accurately predicting frequency and amplitude of oscillation.

© 2018 Elsevier Ltd. All rights reserved.

## 1. Introduction

### 1.1. Importance of dynamic behavior in two-phase thermal management systems

Due to their superior ability to cool high energy density devices, engineers worldwide are considering two-phase flow thermal management systems to tackle the next generation of device cooling challenges [1]. Researchers at the Purdue University Boiling and Two-Phase Flow Laboratory (PU-BTPFL) and other organizations have investigated many different configurations to efficiently utilize phase change heat transfer for thermal management,

including capillary-driven devices [2–4], pool boiling thermosyphons [5–7], falling film [8,9], channel flow boiling [10,11], micro-channel boiling [12–16], jet impingement [17–20], and spray [21–27], as well as hybrid configurations [28–31] involving two or more of these schemes.

Although a capable option for any thermal management challenge, systems capitalizing on phase change heat transfer are particularly attractive options for utilization in aerospace thermal-fluid systems where their orders-of-magnitude improvement in heat transfer coefficient allow for appreciable reductions in size and weight of hardware. Because of this potential, there is a push by space agencies worldwide to develop the technology further and allow implementation in both space vehicles and planetary bases. Current targets for adoption of phase change technologies include Thermal Control Systems (TCSs), which control temperature and humidity of the operating environment, heat

\* Corresponding author.

E-mail address: [mudawar@ecn.purdue.edu](mailto:mudawar@ecn.purdue.edu) (I. Mudawar).

URL: <https://engineering.purdue.edu/BTPFL> (I. Mudawar).

**Nomenclature**

$A$	amplitude		
$Bo$	boiling number		
$Co$	confinement number		
$D_h$	hydraulic diameter		
$f$	frequency		
$Fr_f$	liquid Froude number		
$G$	mass velocity		
$g$	Earth's gravitational constant		
$H$	height of flow channel's cross-section; digital filter transfer function		
$h_{fg}$	latent heat of vaporization		
$L_d$	development length of flow channel		
$L_e$	exit length of flow channel		
$L_h$	heated length of flow channel		
$\dot{m}$	mass flow rate		
$N_{pch}$	phase change number		
$P$	pressure		
$P'$	mean-subtracted pressure fluctuations		
$Q$	total heat input		
$q''$	heat flux on heated perimeter of channel		
$Re_f$	liquid Reynolds number		
$T$	temperature		
$t$	time		
$U_{char}$	characteristic velocity		
$v$	specific volume		
$W$	width of flow channel's cross-section		
$We_f$	liquid Weber number		
$x_e$	thermodynamic equilibrium quality		
$z$	variable indicating digital domain		
		<i>Greek symbol</i>	
		$\mu$	dynamic viscosity
		$\mu_p$	mean of pressure set, statistical parameter
		$\rho$	density
		$\rho_{cc}$	cross correlation coefficient, statistical parameter
		$\sigma$	surface tension
		$\sigma_p$	standard deviation of pressure set, statistical parameter
		<i>Subscripts</i>	
		<i>ave</i>	average
		<i>exp</i>	experimental (measured)
		<i>f</i>	saturated liquid
		<i>g</i>	saturated vapor
		<i>in</i>	inlet to heated portion of channel
		<i>k</i>	Fourier series index
		<i>out</i>	outlet to heated portion of channel
		<i>rec</i>	reconstructed
		<i>SE</i>	single event
		<i>w</i>	wall
		<i>Acronyms</i>	
		CHF	critical heat flux
		DWO	density wave oscillation
		FBM	flow boiling module
		HDF	high density front
		LDF	low density front
		PCI	parallel channel instability
		PDO	pressure drop oscillation

receiver and heat rejection systems for power generating units, and Fission Power Systems (FPSs), which are projected to provide high power as well as low mass to power ratio [32–34].

Unlike most ground-based systems, design of thermal-fluid space systems has the added difficulty of hardware lifecycles encountering a wide range of operating environments. From the hyper-gravity associated with launch, to the micro-gravity of orbit and/or deep space, to the varying gravitational fields associated with operation on various extra-terrestrial bodies, any thermal management system designed for aerospace applications will need to be robust to drastic changes in operating conditions. This is particularly difficult for systems involving phase-change, as phenomena related to buoyancy and surface tension can have large effects on critical aspects of two-phase flow such as flow regime, phase distribution, and even the nucleation process itself. Prior studies conducted with the aid of parabolic flight have shown changes in local acceleration lead to dynamic changes in flow boiling behavior, with similar operating conditions tested in micro-gravity and hyper-gravity environments yielding significant difference in flow boiling heat transfer [35,36].

In addition to alterations in system performance due to direct changes in operating environment (*i.e.*, changes to local acceleration), changes to ambient thermal environment of the system often necessitate changes in operation mode. Be it due to the cyclical nature of solar exposure in orbiting vehicles, differences in ambient temperature between operations in space (transit) and some terrestrial environment (Moon, Mars, *etc.*), or changes in thermal loading due to periodic operation of high-energy instruments, it is likely any dedicated two-phase flow thermal management system will need to operate across a range of flowrates, heat fluxes, and pressures. Many studies have shown how changes to these parameters can instigate the onset of flow boiling instabilities,

expressing transition criteria in the form of both stability maps [37–39] and transition correlations [40–43], but further study of the characteristics of these instabilities and other transient phenomena is necessary.

### 1.2. Flow boiling instabilities and transient phenomena

Due to complex interplay between thermo- and hydro-dynamic effects, two-phase flows with mass transfer (flow boiling, flow condensation) commonly exhibit flow '*instabilities*', which are dynamic, transient events manifesting under certain operating conditions that can impact system performance. The origin of the study of two-phase flow instabilities is commonly attributed to Ledinegg [44], who discovered for certain operating conditions two-phase flow systems experience a jump from an unstable location to a stable location on the system's internal-external pressure curve. This manifests as a change in both system mass velocity and operating pressures.

Several decades later researchers began to investigate less noticeable, more persistent transient phenomena found in two-phase flow systems [45–47], with special attention paid to Density Wave Oscillations (DWOs) [48,49]. It was around the same time that Boure et al. published their seminal review of two-phase flow instabilities [50], which provided the basis for many continuing investigations of dynamic flow behavior in two-phase flow systems. Of key importance from their work is the classification of instability modes based in part on the frequency at which they occur, an attribute investigated extensively in the present study.

Over the ensuing decades through present day, researchers have continued investigating instabilities and transient behavior observed in experimental two-phase flow thermal management systems, focusing on DWOs [51–54], Parallel Channel Instability

(PCI) [55–57], Pressure Drop Oscillations (PDOs) [58–60], and interaction of multiple instability modes [61,62]. Recent reviews, such as those by Tadrist [63], Kakac and Bon [64], and Ruspini et al. [65] provide updated surveys of literature relating to phenomena first reported by Boure et al. [50], including overviews of approaches taken towards modeling their behavior.

Many recent experimental studies concerning two-phase flow heat transfer have also begun to focus more on aspects of transient system behavior other than primary instability modes, centering on bubble dynamics in micro-channels [66], general temperature, pressure, and heat transfer fluctuations [67–71], transient flow pattern transitions [72], and even system response to manually induced periodicity [73]. It is expected that much of the transient behavior observed in these studies can be related to either instabilities present in two-phase flow systems or externally induced oscillations, and adoption of a systematic analysis approach by the two-phase flow community at large could greatly homogenize interpretation of results.

This growing body of work dealing with two-phase flow instabilities and transient behavior has led to broadened understanding of the driving forces behind two-phase flow instabilities and the conditions under which they occur, as well as the need to mitigate them when operating near critical conditions (*e.g.*, critical heat flux (CHF), dryout, or choking). Development of general predictive tools capable of characterizing two-phase flow instabilities is still a deficiency in existing literature, however, with many existing models incorporating experimental results as boundary conditions, making assumptions regarding amplitude of oscillation, or requiring prohibitively large computational resources to provide reasonable prediction of two-phase flow instabilities. Underlying this lack of useful design tools for mitigation of two-phase flow instabilities is the lack of experimental data clearly characterizing key instability features, a deficiency this study aims to help rectify.

### 1.3. Objectives of study

This study is part of an ongoing collaboration between Purdue University Boiling and Two-Phase Flow Laboratory (PUBTFL) and NASA Glenn Research Center (GRC) whose ultimate goal is to develop the Flow Boiling and Condensation Experiment (FBCE) for the International Space Station (ISS). A detailed summary of outcomes from the project thus far, including key objectives, experimental methodology, analytic approaches, and other relevant works, can be found in a recent summary article [74].

The current work deals with flow boiling and augments prior work dealing with experimental investigation and prediction of key design parameters such as heat transfer coefficient [75–78], pressure drop [53,79,80], and critical heat flux [81–87], with a comprehensive analysis of experimental data for DWOs evident in vertical upflow boiling. It also aims to utilize this information to determine any potential impact of DWOs on the operation of FBCE on the ISS. Objectives for analysis are:

- (1) Use transient pressure signals and flow visualization images to provide a comprehensive characterization of DWOs along with a physically consistent explanation for their manifestation in vertical upflow boiling.
- (2) Analyze a large database of vertical upflow cases exhibiting DWO behavior to better draw conclusions regarding trends for frequency and amplitude of DWO induced pressure oscillations.
- (3) Present analysis regarding the viability of reconstructing transient pressure results using detected frequency and amplitude, with the aim of better informing DWO model development.

This work builds directly on prior studies by the current authors [53,54], which established an approach for the characterization of DWOs based on amplitude and frequency of induced pressure oscillations. Great care was taken in isolating physical, dynamic behavior due to DWOs from mechanically-induced oscillatory behavior through careful analysis of transient pressure signals and corresponding fast Fourier transforms, and conclusions from these works provided a starting point from which the present analysis was begun. It should also be noted that this work is the companion study to another [88] presenting a new analytic model for predicting frequency and amplitude of DWOs in vertical upflow boiling.

## 2. Experimental methods

### 2.1. Flow boiling module

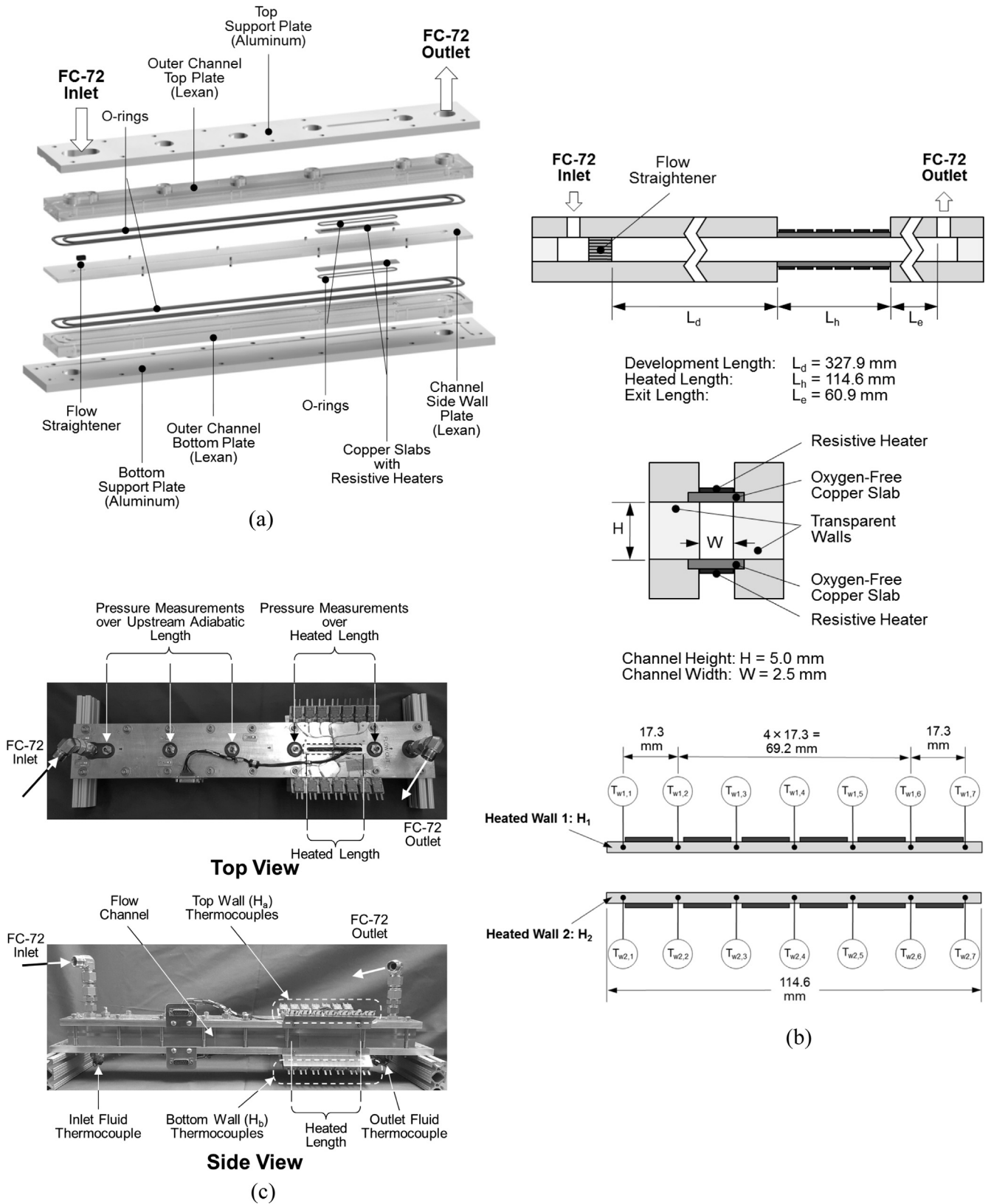
As a part of the FBCE designed towards eventual use on the ISS, the Flow Boiling Module (FBM) is a test section instrumented to allow capture of high-speed photography through transparent polycarbonate sidewalls while simultaneously allowing detailed flow boiling heat transfer and pressure drop measurements to be made over a heated length composed of copper top and bottom walls with resistive heaters soldered to their backs and thermocouples imbedded. Fig. 1(a) illustrates how the FBM is constructed by clamping three pieces of transparent polycarbonate plastic (Lexan) between two aluminum support plates. Although Fig. 1(a) indicates two o-rings are used to seal the fluid path, only one is actually used due to difficulties in assembly with two. Fig. 1(b) shows the middle polycarbonate piece is milled out to create a rectangular 2.5-mm wide, 5-mm tall flow channel with a development length of 327.9 mm followed by a heated length of 114.6 mm, constructed by recessing oxygen-free copper slabs flush with the channel's top and bottom walls. Each copper slab has six 4.5-mm wide, 16.4-mm long, 188- $\Omega$  resistive heaters soldered to their backs, evenly spaced with small gaps between successive heaters to allow temperature measurements to be made using type-E thermocouples. Heat flux to each wall can be controlled separately, although the present study deals only with cases where heat is supplied evenly to both heated walls.

Fig. 1(c) shows images of the actual FBM with key points identified. The top view shows the five pressure measurement points, comprised of three along the development length, one upstream of the heated length, and one downstream of the heated length. Fig. 1(c) also illustrates the location of inlet and outlet fluid temperature measurements, performed using type-E thermocouples inserted directly into the flow.

### 2.2. Flow boiling test loops

The present study utilizes results from two separate sets of flow boiling experiments performed over a two-year period (2015 and 2016), both performed with FBM as test module, but using different peripheral equipment. Based on conclusions from a proceeding study by the present authors [54], DWO induced behavior within the test section was seen to be largely independent of component selection within the flow loop, meaning the comparison of experimental results from the two studies constitutes a good check for the repeatability of DWOs across separate test runs with similar operating conditions.

Fig. 2(a)–(d) provides both schematics and photos of hardware used in each respective set of experiments. In both cases, an Ismat-ech MCP-z magnetically-coupled gear pump is used to circulate the



**Fig. 1.** (a) Exploded view of the flow boiling module (FBM). (b) Schematics of FBM fluid path and heated wall temperature measurement locations. (c) Photos of FBM with key components labeled.

working fluid, FC-72, through the system. Exiting the pump, the fluid passes through a filter to remove any particulates before entering a turbine flow meter for flow rate measurement. After

the flow meter, the fluid enters the bulk heater(s) where power is supplied to set the fluid's thermodynamic conditions before entering the FBM.

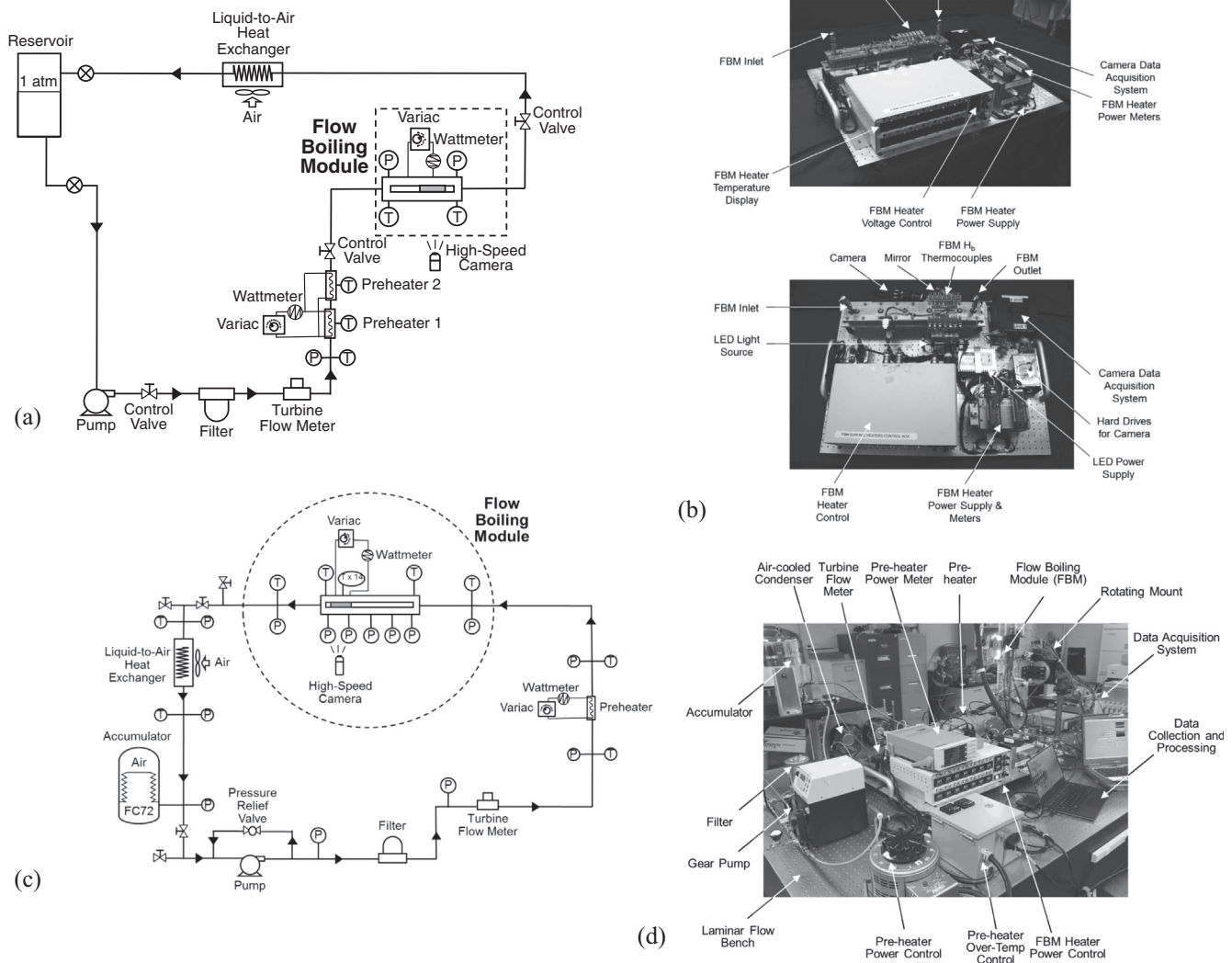


Fig. 2. (a) Schematic and (b) photos of year 1 (2015) experimental flow boiling facility, and (c) schematic and (d) photo of year 2 (2016) experimental flow boiling facility.

In both sets of experiments wall heat flux in the flow boiling module is controlled using the FBM heater control module, which also ensures the module's safety by automatically disabling the power supply should any of the heated wall temperatures exceed 125 °C (occurring only during the CHF transient). Upon exiting the test section, the fluid passes through a condenser to return to a subcooled, single-phase liquid state before entering the pump.

Key differences to note between the two systems are:

- (1) The use of two small Cast-X bulk heaters in Fig. 2(a) versus one larger Cast-X bulk heater in Fig. 2(c).
- (2) A liquid-to-liquid heat exchanger is used to condense the fluid in Fig. 2(a), versus a liquid-to-air heat exchanger in Fig. 2(c).
- (3) Use of a reservoir in Fig. 2(a) versus an accumulator in Fig. 2(c).

It is also worth noting that the system used in year 2 (2016) and depicted schematically in Fig. 2(c) contains a far greater number of pressure transducers throughout the loop to better assess the impact of different system components of flow dynamic behavior.

Data throughout both systems are obtained with an NI SCXI-1000 data acquisition system controlled by a LabVIEW code. Pressure transducers are sampled at 200 Hz, allowing high fidelity transient analysis of pressure signals.

Images are captured at a rate of 2000 frames per second (fps) with a pixel resolution of 2040 × 156 spanning the total 114.6-mm heated length. Illumination is provided from the opposite side of the flow channel by blue LEDs, with light passing through a light shaping diffuser (LSD) to enhance illumination uniformity.

### 2.3. Operating conditions and measurement uncertainty

Full operating conditions for each set of experiments conducted and details regarding operating procedure can be found in the original experimental studies associated with each [53,54]. The subset of operating conditions used for the present study is provided in Table 1, and corresponds to the full range of operating conditions (mass velocities, inlet qualities, heat fluxes, and inlet pressures) for which DWOs are observed in vertical upflow orientation. As discussed in [54], DWOs do not manifest in the current test geometry for highly subcooled inlet conditions, so all cases presented here correspond to finite inlet qualities. Further, only vertical

**Table 1**  
Operating conditions used in present study.

Experiment subset	$G$ [kg/m <sup>2</sup> s]	$x_{e,in}$	$q''$ [W/cm <sup>2</sup> ]	$P_m$ [kPa]	Datapoints
Year 1 (2015)	190.7–1978.9	0.00–0.69	1.0–22.5	109.7–190.3	192
Year 2 (2016)	199.5–808.8	0.00–0.18	0.0–28.3	130.7–229.3	44
Overall	190.7–1978.9	0.00–0.69	0.0–28.3	109.7–229.3	236

upflow is selected to limit analysis to a commonly employed flow boiling orientation for Earth-based systems.

Type-E thermocouples with an accuracy of  $\pm 0.5$  °C are used to measure fluid and heated wall temperatures throughout the facility. Pressure measurements throughout the flow loop are made using pressure transducers with an accuracy of  $\pm 0.1\%$ , which corresponds to an accuracy for all pressure drop measurements of  $\pm 0.2\%$ . Pressure transducers used in the present study possess a mechanical response time of less than 1 ms, allowing the signal to be sampled at 200 Hz (once every 0.005 s). The turbine flow meter has an accuracy of  $\pm 0.1\%$ . The wall heat input is measured with an accuracy of  $\pm 0.5$  W.

### 3. Analysis of density wave oscillation (DWO) phenomenon

#### 3.1. Density wave oscillations (DWOs) in micro-channels versus mini/macro-channels

In many prior works [49–52] DWOs have been explained as resulting from delay and feedback effects between thermal and hydrodynamic phenomena present within two-phase flows. In micro-channels, the phenomenon leading to DWOs is easily visible, as large values of confinement number,

$$Co = \frac{\sqrt{\frac{\sigma}{g(\rho_f - \rho_g)}}}{D_h} \quad (1)$$

representing the ratio of Taylor Wavelength to channel hydraulic diameter, lead to vapor formation via nucleation on a scale comparable to the hydraulic diameter. This displaces significant amounts of liquid within the channel, and can cause instantaneous mass conservation imbalances between the channel inlet and outlet, leading to a surge of liquid (and associated pressure drop) which ensures continuity is satisfied in time-averaged fashion.

In mini/macro channels (such as in the present FBM), however, vapor generation through nucleation is not of a scale comparable to hydraulic diameter, meaning other explanations must be present for the pressure and flowrate oscillations experimentally detected and associated with DWOs. This also severely limits the applicability of some existing correlations for frequency of oscillatory behavior, such as those recently investigated by Lee et al. [60] for pressure oscillations in micro-channel boiling, which depend primarily on the nucleation process and associated surface tension effects.

Classic mini-channel DWO studies, such as the works of Ishii [89], Belblidia and Bratianu [90], and Lahey and Podowski [47], dealt primarily with subcooled flow boiling and attributed low-frequency oscillations in pressure and flowrate to feedback between changes in system pressure and thermophysical properties. In a simple example, an increase in system pressure would lead to a change in position of the Onset of Nucleate Boiling (ONB) point, which would change the pressure-drop characteristics of the system, causing the system pressure to drop, the ONB point to change in the opposite direction, and the process to repeat itself.

These works included extensive analysis, primarily focused on development of full two-phase flow field models (slip flow, drift flux, even homogeneous equilibrium model) and applying classic

stability theory to governing equations to determine stability boundaries, leading to the development of stability maps such as that of Ishii and Zuber [37] (developed for use with the experimental data of Solberg [91]).

This classic analysis does not fit well with experimental data observed by the present authors in a prior study [54], however, which saw little appreciable oscillatory behavior in the relevant frequency range ( $\sim 0.5$ – $10$  Hz) for subcooled flow boiling in the FBM. Indeed, the recent review of Ruspini et al. [65] indicated the presence of three ‘types’ of DWOs in the literature: Type 1, due to gravity, Type 2, due to friction, and Type 3, due to momentum. The underlying idea is DWOs could be formed by different combinations of forces/driving behaviors depending on operating conditions and test section geometry, with all eventually yielding oscillations in the low frequency range.

This dependence on operating conditions for both when and how DWOs manifest is more accommodating to experimental conditions such as those in [54] which do not fit the classical description of DWOs well, but nonetheless exhibit strong signs of oscillatory behavior commonly attributed to DWOs. In keeping with this, the present study will neglect the classic analysis approach and focus on determining the mechanisms behind formation of DWOs by starting from flow visualization images and applying analysis focused on perceived dominant hydrodynamic and thermodynamic effects during the DWO process (*i.e.*, body force, phase change, *etc.*).

It should be noted, prior to beginning analysis of experimental results in the present section leading up to the presentation of a comprehensive mechanistic description of the process through which DWOs occur in mini/macro-channels similar to the current configuration, that significant effort has been made in a prior study by the current authors [54] to isolate DWO behavior from transient phenomena artificially induced by mechanical components (*e.g.*, pump operating frequency, condenser fan vibrations, *etc.*). The prior work should be consulted if additional distinction between DWO induced oscillations and other fluctuations present in two-phase flow systems is necessary.

#### 3.2. Analysis of transient pressure signals

As shown in prior works [53,54], a first step in determining the presence and impact of DWOs within a system is analysis of transient pressure results. A prior study by the present authors [54] investigated changes in other key parameters such as mass velocity and temperature along with pressure in cases with and without DWOs present, but for the present work analysis will be limited to transient pressure signals as it has been shown to most clearly illustrate the presence and influence of DWOs within the system.

Fig. 3(a)–(c) provides transient pressure results corresponding to measurement locations at the inlet and outlet of the FBM’s heated length, along with Fourier transforms of each signal, for mass velocities of  $G = 234.2$  kg/m<sup>2</sup> s, 834.1 kg/m<sup>2</sup> s, and 1978.9 kg/m<sup>2</sup> s, respectively, all gathered during year 1. It should be noted that, for each subfigure, two transient plots are provided: one encompassing the entire 20-s period used to perform the fast

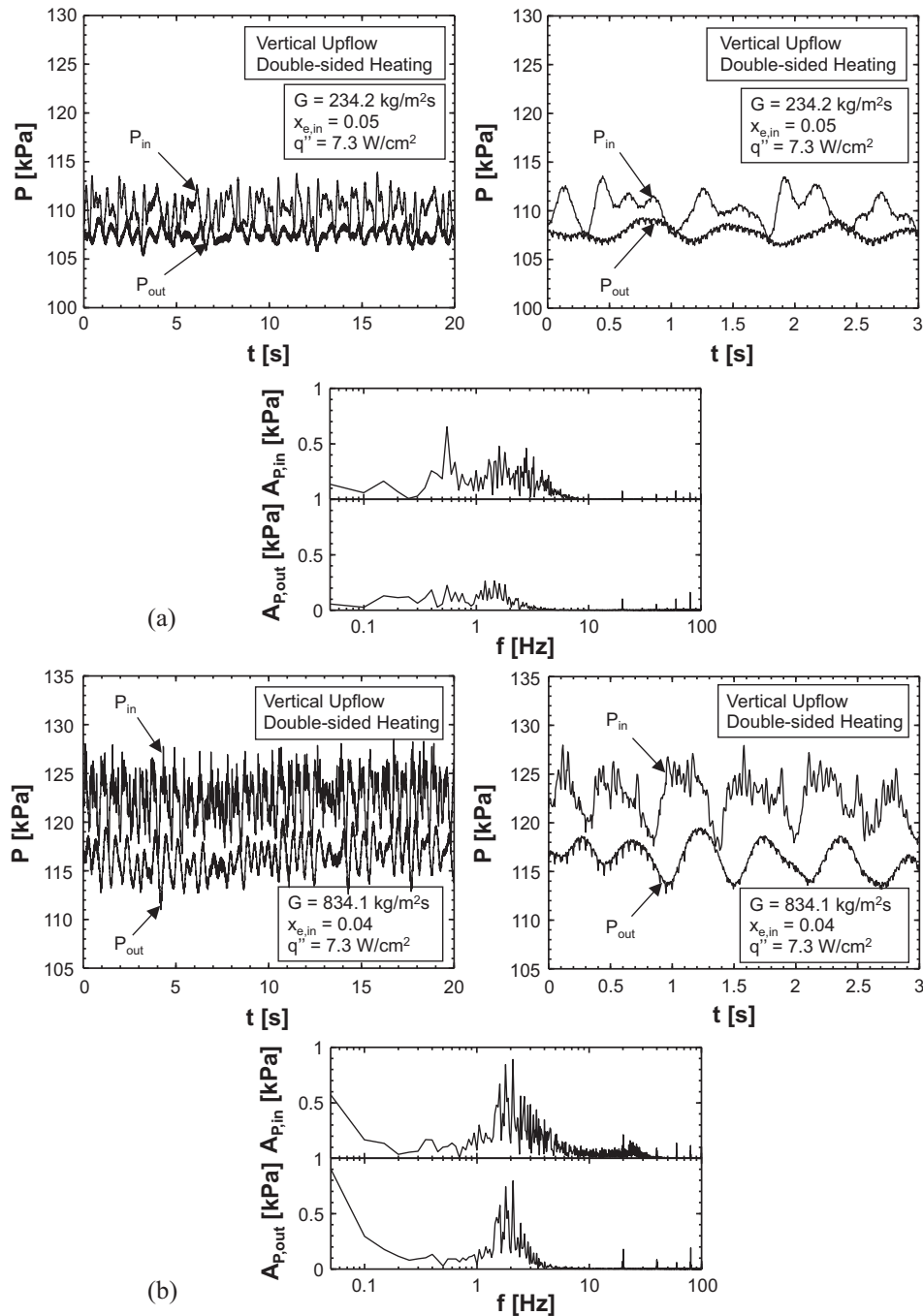


**Fig. 3.** Plots of FBM heated length inlet and outlet pressures versus time over 20 s, zoomed in on the first 3 s, and associated fast Fourier transforms over the 20-s period for (a)  $G = 234.2 \text{ kg/m}^2 \text{ s}$ , (b)  $G = 834.1 \text{ kg/m}^2 \text{ s}$ , and (c)  $G = 1978.9 \text{ kg/m}^2 \text{ s}$ .

Fourier transform, and another displaying only the first 3 s of data to better highlight characteristics of each individual curve.

Fig. 3(a) shows that, for the lowest mass velocity of  $G = 234.2 \text{ kg/m}^2 \text{ s}$ , both inlet and outlet pressure signals exhibit behavior indicative of DWOs in the 0.5–5 Hz frequency range. It is clear, however, that the inlet pressure signal experiences significantly larger fluctuations, and these fluctuations are sharper in nature. The short-duration transient plot clearly displays near-sinusoidal behavior by the outlet pressure, while the inlet pressure seems to be characterized more by sharp departures from a nominal value. This type of oscillatory behavior is periodic in nature but

not perfectly sinusoidal, a distinction which will become important in later analysis.

Fig. 3(b), corresponding to the moderate mass velocity of  $G = 834.1 \text{ kg/m}^2 \text{ s}$ , shows that as mass velocity is increased larger pressure fluctuations are seen at both inlet and outlet. Similar to Fig. 3(a), the outlet pressure behaves in a near-sinusoidal fashion, while the inlet is characterized by sharp departures from a nominal level. This difference in behavior is also clearly manifest in the frequency composition of each signal, with both inlet and outlet pressures exhibiting a peak at  $\sim 2 \text{ Hz}$ , but with significantly more spread in frequency composition seen in the inlet signal as compared to

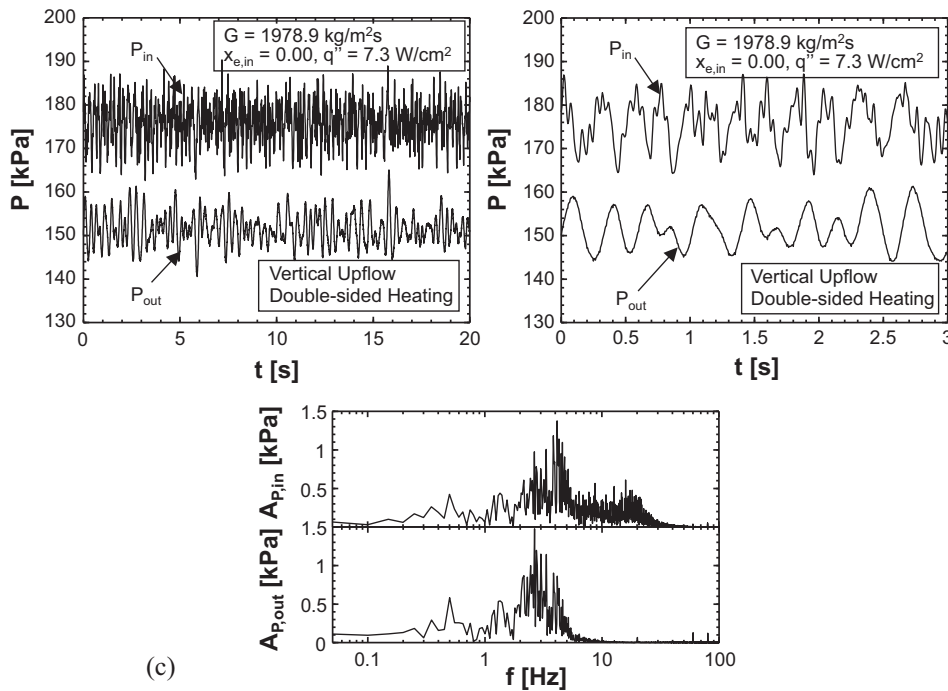


Fig. 3 (continued)

the outlet signal. Also of interest is the clear presence of a slight phase shift between inlet and outlet pressures when analyzing the short-duration transient plot. Peaks in inlet pressure are followed shortly by peaks in outlet pressure, and troughs in inlet pressure lead to troughs in outlet pressure shortly after. The fact that these two pressure measurement locations do not exhibit in-phase fluctuations indicates the passage of a transient through the heated length of the test section.

Fig. 3(c) reinforces the trends evident in the first two subfigures by providing similar results for the highest mass velocity case of  $G = 1978.9 \text{ kg/m}^2 \text{ s}$ . Similar to Fig. 3(a), peak frequencies of oscillation for inlet and outlet pressures differ slightly.

Across all three subfigures for the present operating conditions corresponding to finite quality flow within the test section at various pressures and mass velocities DWOs are seen to manifest. Differences are present when comparing inlet and outlet pressure curves for certain cases, however, primarily in frequency of oscillation. This is likely due to some combination of thermal and hydrodynamic effects taking place within the heated length of the test section, and is indicative of DWOs being characterized by passage of a transient through the system.

### 3.3. Flow visualization images

Although imaging of two-phase flow with finite quality often yields inferior results to that of subcooled boiling due to the necessity of imaging through a disturbed liquid film (as is the case for annular flow), important conclusions regarding the formation and occurrence of DWOs in the present system may be drawn nonetheless through careful analysis of flow visualization sequences. Although mentioned when discussing experimental methods, it should be noted again that images presented here correspond to the entire 114.6-mm heated length of the FBM and are captured at a rate of 2000 fps with an electronic resolution of  $2040 \times 174$  pixels. Additionally, all images presented within the present section correspond to tests performed during year 1.

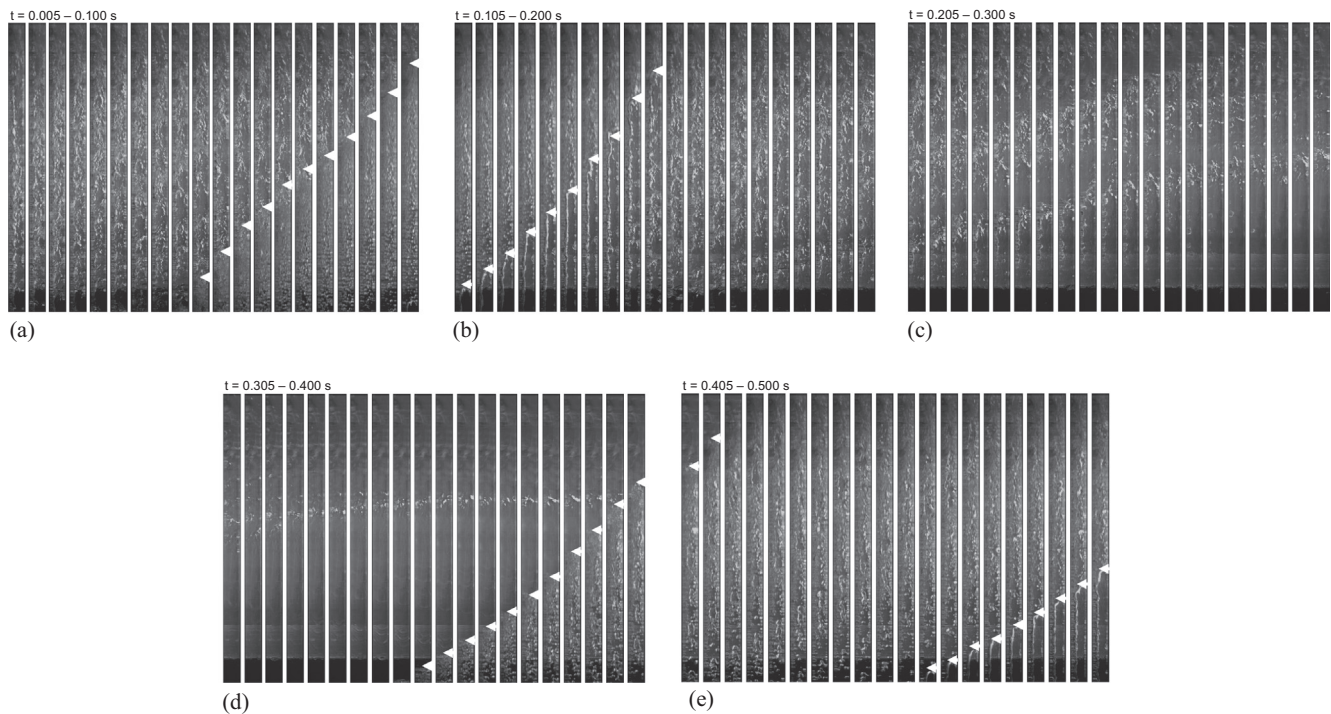
Fig. 4(a)–(e) depicts five sequences of images for a test case corresponding to mass velocity of  $G = 407.8 \text{ kg/m}^2 \text{ s}$ , inlet quality  $x_{e,in} = 0.03$ , average inlet pressure  $P_{in} = 116.0 \text{ kPa}$ , and heat flux  $q'' = 7.2 \text{ W/cm}^2$ . Each consecutive set of images is separated by 0.005 s, and the entire range of images across Fig. 4(a)–(e) corresponds to a single consecutive set of images spanning 0.5 s of real-time.

Fig. 4(a) illustrates that, for an arbitrary starting point selected within the imaging sequence, flow through the heated length of the test section is nominally annular. However, as time progresses, a point is reached at which flow into the heated length is no longer annular, but is instead largely liquid. This point is indicated in Fig. 4(a) with a white arrow. As time advances further, this front (still indicated by a white arrow) is seen to move along the length of the channel, with nucleate boiling now taking place within the liquid as opposed to film evaporation common to annular flow.

Just prior to the transition from Fig. 4(a)–(b), it can be seen that the entire channel length becomes occupied by liquid, with subcooled boiling taking place along the heated walls. At the start of Fig. 4(b), however, a pocket of vapor is clearly seen to begin working its way along the channel length, highlighted again by a white arrow. As the front of the vapor pocket moves along the channel length, it begins to lose its crisp boundary, instead devolving back into annular flow, evident from the increased presence of interfacial waves which are a key characteristic of vapor core flow past a liquid film. Annular flow continues to dominate throughout Fig. 4(b), similar to the flow conditions present within Fig. 4(a).

Just prior to transitioning to Fig. 4(c), however, the liquid film in the entrance region begins to show signs of drying out. This continues throughout Fig. 4(c), with significantly reduced liquid content present in the heated length of the channel, and, by the time Fig. 4(d) is reached, the heated length becomes almost entirely devoid of liquid.

Halfway through Fig. 4(d), however, another liquid wetting front emerges, clearly indicated with white arrows. This high density front advances along the channel length, with nucleate boiling taking place within it similar to the behavior seen in the latter half



**Fig. 4.** Consecutive flow visualization image sequences for vertical upflow boiling with  $G = 407.8 \text{ kg/m}^2 \text{ s}$ ,  $x_{e,in} = 0.03$ ,  $P_{in} = 116.0 \text{ kPa}$ , and  $q'' = 7.2 \text{ W/cm}^2$ , spanning (a) 0.005–0.100 s, (b) 0.105–0.200 s, (c) 0.205–0.300 s, (d) 0.305–0.400 s, and (e) 0.405–0.500 s. Time difference between consecutive image sequences is  $\Delta t = 0.005 \text{ s}$ .

of Fig. 4(a). As the front reaches the end of the heated length increased vapor content causes it to transition away from sub-cooled boiling of the liquid slug towards annular flow with film boiling as seen in Fig. 4(b).

This behavior continues for the first portion of Fig. 4(e), until roughly halfway through another vapor (low density) front emerges at the inlet of the channel, clearly indicated with white arrows. This repetition of behavior seen in Fig. 4(b) indicates the passage of high density (liquid) and low density (vapor) fronts, with annular flow occupying the interim periods, is a cyclical process.

Fig. 5(a)–(e), displaying flow visualization image sequences for the higher mass velocity of  $G = 821.6 \text{ kg/m}^2 \text{ s}$ , inlet quality  $x_{e,in} = 0.06$ , average inlet pressure  $P_{in} = 123.8 \text{ kPa}$ , and heat flux  $q'' = 7.2 \text{ W/cm}^2$ , further reinforces the concept that the passage of high and low density fronts is cyclical in nature. Within each subfigure clear regions of annular flow (characterized by the presence of interfacial waves) give way to the passage of darker colored regions comprised of liquid distributed throughout the cross-sectional area of the channel. These features are clearly identified with white arrows in Fig. 5(a).

Fig. 5(b) and (c) also shows signs of the passage of high density fronts, but these are much smaller in size than those seen in Fig. 5(a). Not until Fig. 5(d) is another high density front of significant length observed, again marked by white arrows.

Similarly, Fig. 6(a)–(e) present flow visualization images for the highest mass velocity of  $G = 1636.5 \text{ kg/m}^2 \text{ s}$ , inlet quality  $x_{e,in} = 0.01$ , average inlet pressure  $P_{in} = 154.6 \text{ kPa}$ , and heat flux  $q'' = 7.2 \text{ W/cm}^2$ , in which alternating passage of high and low density fronts can clearly be seen. Beginning with Fig. 6(a), where the front and back of the first two high density fronts are indicated with white arrows, every subfigure shows some indication of alternating high and low density zones.

The possible exception to this is Fig. 6(d), which seems to exhibit a largely constant flow composition over its 0.1-s duration. Although flow regimes are more difficult to distinguish here as

compared to lower flow velocity cases, annular flow seems to dominate in Fig. 6(d), evidenced by the presence of dark, wavy features in the near-wall region. This reinforces the notion that annular, co-current flow is the nominal flow configuration for these cases.

Across Figs. 4–6, flow visualization image sequences indicate the clear presence of cyclical passage of high and low density fronts through the heated length of the test module, with annular flow providing a neutral state between the two. Recalling the clear periodic behavior seen within transient pressure signals in Fig. 3, it can be hypothesized that the two phenomena are interrelated, and that the cyclical passage of high and low density fronts are the cause of low frequency oscillatory behavior attributed to DWOs.

All of this information is combined in Fig. 7(a)–(c), which display, respectively, select flow visualization images, a table of single-event frequencies for the cyclical passage of high and low density fronts, and transient pressure results for  $G = 1221.9 \text{ kg/m}^2 \text{ s}$ , inlet quality of  $x_{e,in} = 0.02$ , average inlet pressure of  $P_{in} = 129.1 \text{ kPa}$ , and heat flux of  $q'' = 7.3 \text{ W/cm}^2$ . After identifying the passage of high density fronts within high speed flow visualization images as shown in Fig. 7(a), single event frequencies can be found, with single event frequency  $f_{SE}$  defined as

$$f_{SE} = \frac{1}{t_{HDF,2} - t_{HDF,1}}, \quad (2)$$

where  $t_{HDF,2}$  and  $t_{HDF,1}$  refer to the times (relative within the image sequence) at which the first and second high density fronts (HDFs) are observed passing through the test section, respectively. Some values for single even frequency are tabulated in Fig. 7(b).

These values can be compared to the peaks in amplitude versus frequency plots provided for the associated transient pressure curves in Fig. 7(c), presented in a fashion identical to that in Fig. 3. The peak frequency of oscillation for inlet pressure in this case falls between 3 and 4 Hz, while for the outlet pressure it is between 2 and 3 Hz. Tabulated values for  $f_{SE}$  in Fig. 7(b) fall within the range of 4–7 Hz, which are slightly higher than the peak

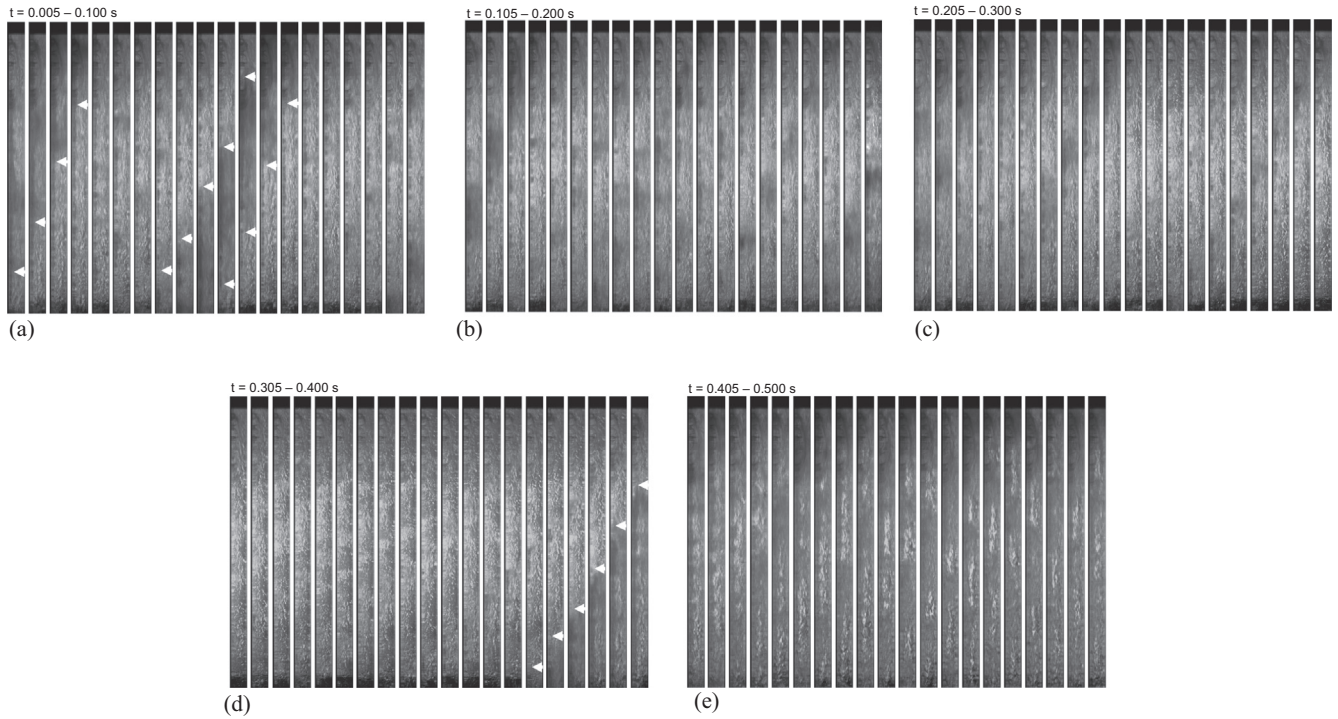


**Fig. 5.** Consecutive flow visualization image sequences for vertical upflow boiling with  $G = 821.6 \text{ kg/m}^2 \text{ s}$ ,  $x_{e,in} = 0.06$ ,  $P_{in} = 123.8 \text{ kPa}$ , and  $q'' = 7.2 \text{ W/cm}^2$ , spanning (a) 0.005–0.100 s, (b) 0.105–0.200 s, (c) 0.205–0.300 s, (d) 0.305–0.400 s, and (e) 0.405–0.500 s. Time difference between consecutive image sequences is  $\Delta t = 0.005 \text{ s}$ .

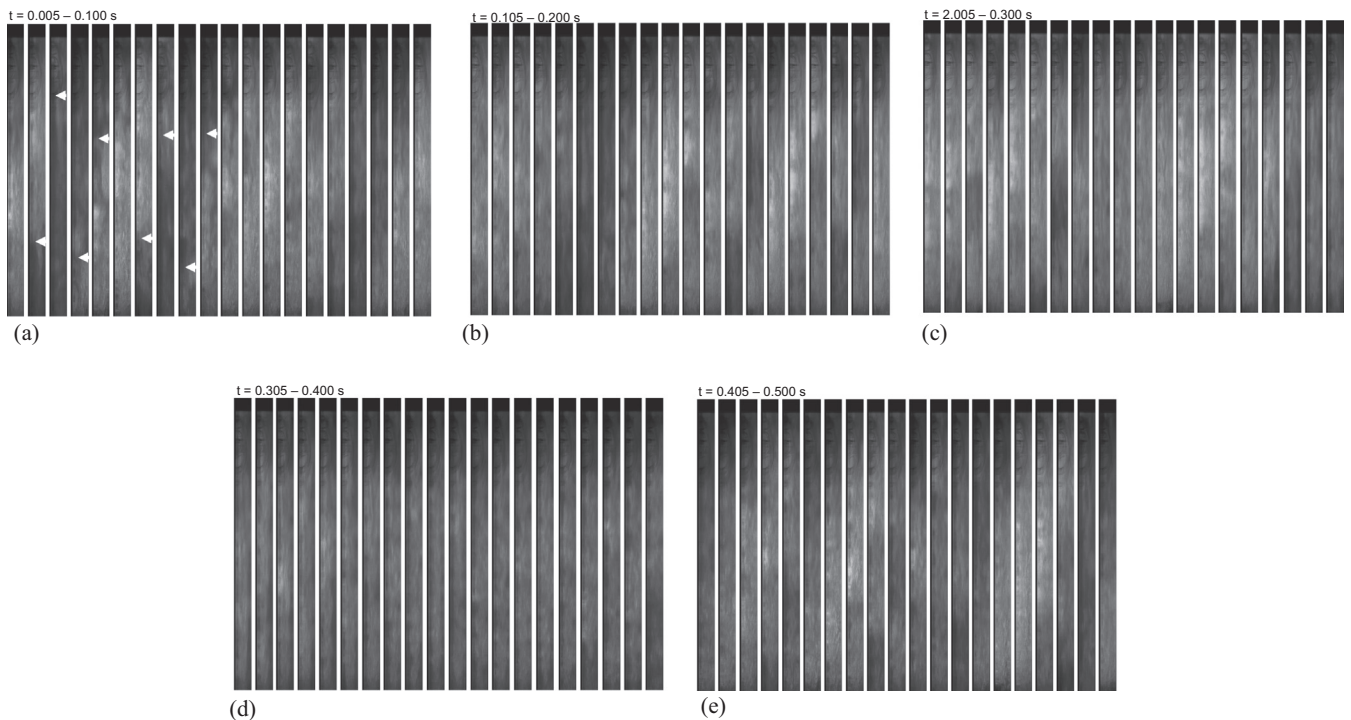
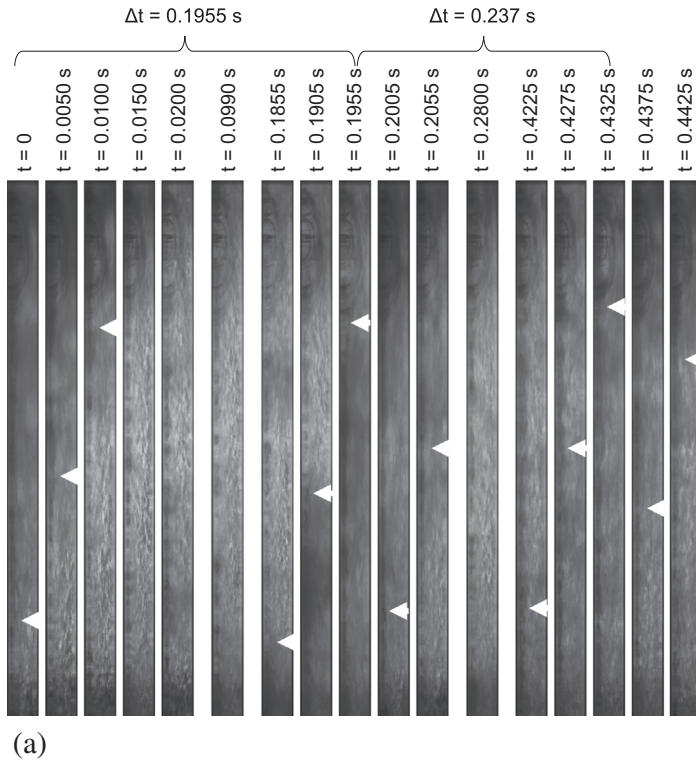


**Fig. 6.** Consecutive flow visualization image sequences for vertical upflow boiling with  $G = 1636.5 \text{ kg/m}^2 \text{ s}$ ,  $x_{e,in} = 0.01$ ,  $P_{in} = 154.6 \text{ kPa}$ , and  $q'' = 7.2 \text{ W/cm}^2$ , spanning (a) 0.005–0.100 s, (b) 0.105–0.200 s, (c) 0.205–0.300 s, (d) 0.305–0.400 s, and (e) 0.405–0.500 s. Time difference between consecutive image sequences is  $\Delta t = 0.005 \text{ s}$ .

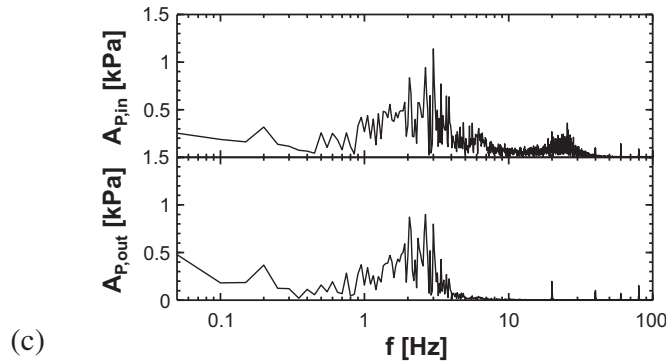
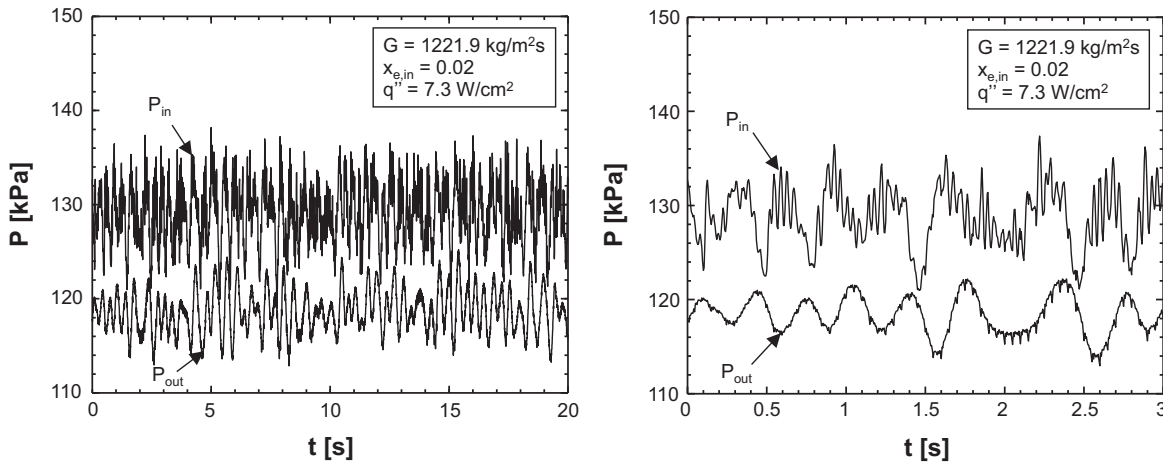
frequencies present after taking a Fourier transform of the experimental data, although still very close. The failure to align exactly with the peak frequencies shown in Fig. 7(c) can be attributed to the fact that the fast Fourier transform performed to produce the amplitude versus frequency plots shown is conducted over a 20-s

period, while the single event frequencies were evaluated over a period of only 0.735 s. High speed imaging was limited to short durations due to data storage limitations, but, were it possible to evaluate single-event frequencies over a similar 20-s period, it is likely the statistical distribution of  $f_{SE}$  would begin to match the



High Frequency Front Occurrence	Time [s]	$\Delta t$ [s]	$f$ [Hz]
1	0.000	-	-
2	0.1955	0.1955	5.11
3	0.4375	0.2420	4.13
4	0.5900	0.1525	6.56
5	0.7350	0.1450	6.90

(b)



(c)

**Fig. 7.** (a) Select flow visualization images for  $G = 1221.9 \text{ kg/m}^2 \text{ s}$ ,  $x_{e,in} = 0.02$ ,  $P_{in} = 129.1 \text{ kPa}$ , and  $q'' = 7.3 \text{ W/cm}^2$  depicting the cycle of low density (bright) fronts and high density (dark) fronts passing through the heated length of the FBM. (b) Tabulated values of single-event frequencies of high density fronts (HDFs) identified from the images and time between HDFs. (c) Transient pressure signals and corresponding fast Fourier transforms confirming the frequencies in (b).

amplitude versus frequency plots in Fig. 7(c) exactly (similar to the result seen when analyzing year 2 images in [54]). It is expected future experiments may not face these imaging duration

limitations and will help provide full validation that dominant low-frequency pressure oscillations are a direct result of the passage of HDFs.

### 3.4. Explanation of density wave oscillation phenomenon

Having used both transient pressure results and flow visualization image sequences to describe the characteristics of DWOs within the present system and prove that pressure fluctuations in the low-frequency ( $\sim 0.5$ – $10$  Hz) range can be associated with cyclical passage of high and low density fronts (regions comprised of mostly liquid and mostly vapor, respectively), it is now possible to present a comprehensive overview of the DWO process. Before embarking, however, it should again be noted that this analysis applies to mini/macro-channels, and DWO formation and behavior in micro-channels is fundamentally different, something briefly discussed in a recent study by Lee et al. [60].

Fig. 8 provides detailed schematics outlining the process by which DWOs occur in vertical upflow boiling. Fig. 8(a) depicts the nominal operating state for finite inlet quality vertical upflow boiling. Key features include annular flow with a vapor core and liquid film distributed around the channel circumference. Phase change takes place along the heated length, manifesting as either nucleate boiling within the liquid film or evaporation at the liquid-vapor interface, depending on film thickness and heat flux applied.

Due to the  $\sim 3$  order of magnitude difference in body force acting on the liquid film versus that on the vapor core, as well as the relatively large size of the channel hydraulic diameter compared to the length scales on which surface tension effects are relevant (quantifiable using Eq. (1)), significant flow separation effects are able to manifest. Interfacial shear stress, acting due to the fast moving vapor core flowing past the slower liquid film, becomes insufficient to overcome body force effects, and the liquid film reaches an unsustainable thickness for annular co-current flow.

Fig. 8(b) shows body force effects causing liquid film accumulation in the inlet region of the channel, leading to increased vapor content and reduced liquid content in the downstream portion of the test module. These conditions correspond to the observation of a low density front (LDF) within the heated length. During this period, mass accumulation takes place within the channel, as mass flowrate of low density vapor at the channel outlet is unequal to the combination of liquid and vapor entering the channel. Correspondingly, momentum inflow is greater than outflow, with the difference being stored in the liquid accumulating near the inlet, which begins to gradually advance downstream.

Fig. 8(c) depicts the motion of this accumulated liquid (high density front, HDF) towards the channel exit. At this point liquid content in the downstream region is at a minimum, a behavior clearly noted in Fig. 4(c) and (d). Additionally, although the HDF is in motion, mass is still accumulating within the channel and net momentum imbalance continues to contribute to its motion. The motion of the HDF itself is extremely complex, as inlet flow to the test section acts as a pseudo-jet impinging on its upstream side, while downstream it is either overtaking flow or being 'stretched', depending on relative velocity of the front and the downstream flow. Body force effects also oppose its motion, while it receives assistance from pressure gradient forces. Perhaps most complicated of all is its interaction with the channel wall(s). Ostensibly, shear stress acts to impede motion of the HDF, but the presence of a residual thin liquid film which is 're-wet' (increased in thickness) and accelerated by residual liquid pulled from the front by surface tension forces indicate wall shear stress may play a minor role in comparison to virtual mass force.

Fig. 8(d) shows the high density front reaching the heated length of the test section, wherein vigorous phase change takes place. In its wake the liquid film has been reestablished along the channel length, and the same can be seen for the heated length as it reaches the end of the channel. Passage of the HDF from the exit of the channel ensures mass conservation is

satisfied, if only in a time-averaged fashion over the duration of the DWO process.

Finally, Fig. 8(e) illustrates a return to nominal operating conditions, from which the process may begin again.

It should be noted that the schematics presented in Fig. 8(a)–(e) correspond to operating conditions similar to those in Fig. 4, where clear boundaries between the liquid and vapor phases are present. For higher flow velocities and/or higher inlet qualities, the combination of increased flow velocity, flow acceleration due to increased void fraction, and decreased liquid content are not conducive to clearly defined phase boundaries for LDFs and HDFs, which is instead manifest as distributed regions of low and high density (seen as light and dark fronts in Figs. 5–7). The mechanisms behind their formation and propagation through the channel, however, remain the same.

It is also worth commenting on the role of body force as a driving mechanism for the formation of DWOs under the present operating conditions. Pressure fluctuations attributable to DWOs have been seen in prior works for multiple orientations in Earth's gravity [53,54] other than vertical upflow, indicating this phenomenon occurs in other orientations due to either other forms of body force influence (liquid-motion assist in vertical downflow, flow stratification in horizontal flow), or the presence of tubes through which two-phase vertical upflow occurs prior to the test section in these orientations. In a micro-gravity environment, however, it is possible the present instability mode may not manifest due to the absence of body force. The upcoming Flow Boiling and Condensation Experiment (FBCE) on the International Space Station (ISS) represents possible proof or disproof of this hypothesis.

## 4. Frequency and amplitude of density wave oscillations

### 4.1. Detection method for frequency and amplitude of oscillation

Having established the process by which DWOs manifest in vertical upflow boiling in mini/macro-channels, analysis can be performed on how frequency and amplitude at which they occur change in response to changes in operating conditions. Prior to this, it is necessary to describe how frequency and amplitude of oscillation are detected.

Fig. 9(a) shows transient pressure curves for the same case as Fig. 3(b), corresponding to operating conditions of  $G = 834.1$  kg/m<sup>2</sup> s,  $x_{e,in} = 0.04$ ,  $P_{in} = 122.6$  kPa, and  $q'' = 7.3$  W/cm<sup>2</sup> observed in year 1. Fast Fourier transforms are performed on these transient pressure signals, with the results shown in Fig. 9(b). Peak frequency of oscillation can be found for both inlet and outlet pressure signals by searching for the frequency associated with peak amplitude of oscillation. It should be noted that the search is limited to frequencies in the relevant range ( $\sim 0.1$ – $10$  Hz) to eliminate the false detection of frequencies associated with non-DWO behavior.

For this set of conditions, Fig. 9(b) indicates that both inlet and outlet pressures oscillate with a peak frequency of 2.1 Hz, associated with an amplitude of  $\sim 0.9$  kPa on the amplitude versus frequency plots. From the transient curves in Fig. 9(a), however, it is clear that pressures oscillate with much higher amplitudes, closer to  $\sim 10$  kPa. This difference is attributed to the combination of two effects. First, as discussed in conjunction with Fig. 7, DWOs do not occur at a constant frequency but over a narrow range of frequencies. Second, and more importantly, DWOs are not perfectly sinusoidal in behavior. As was discussed when presenting Fig. 3, inlet pressures in particular seem to exhibit sharp periodic departures from a nominal level. This behavior is periodic and can be associated with a frequency, but does not exhibit the type

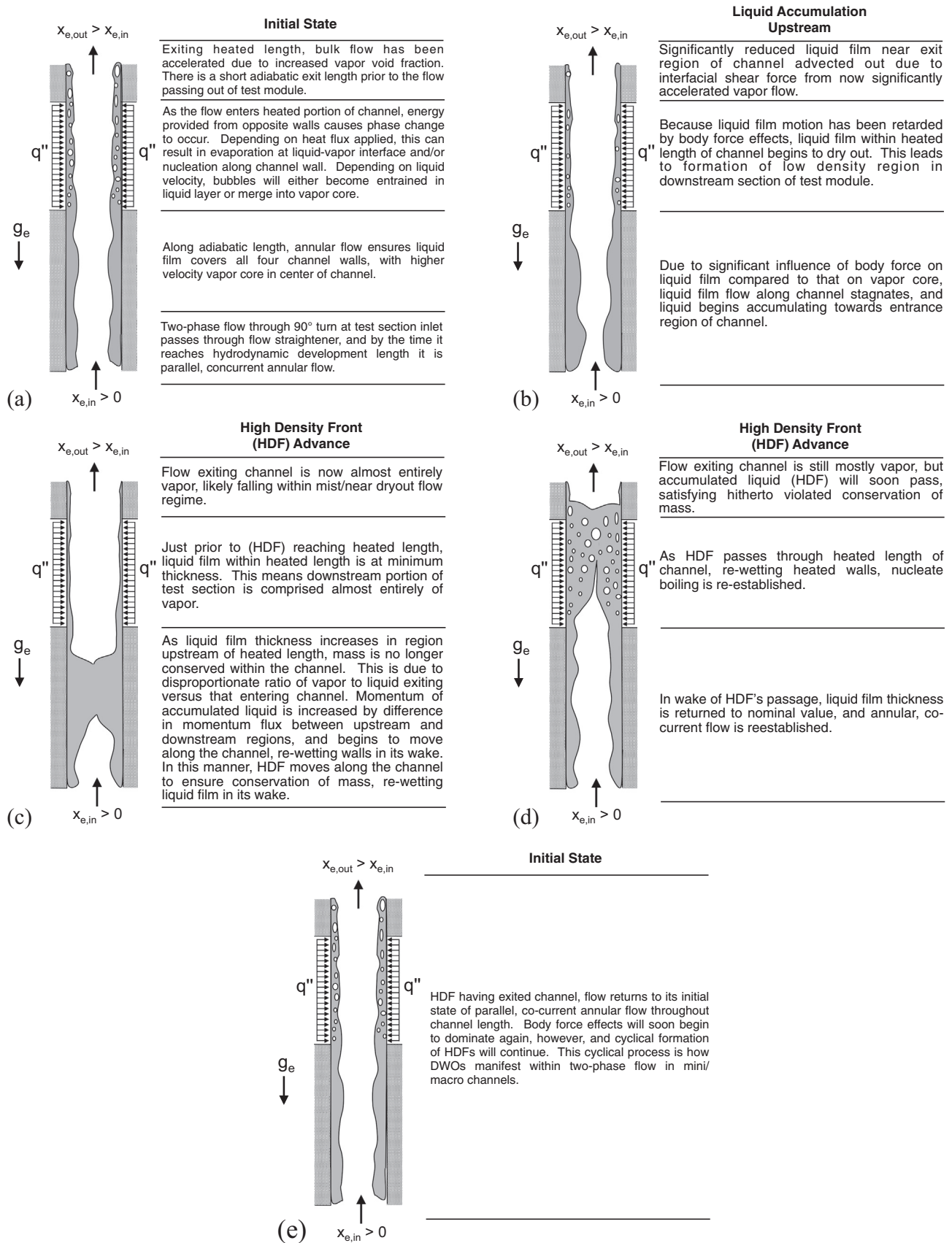
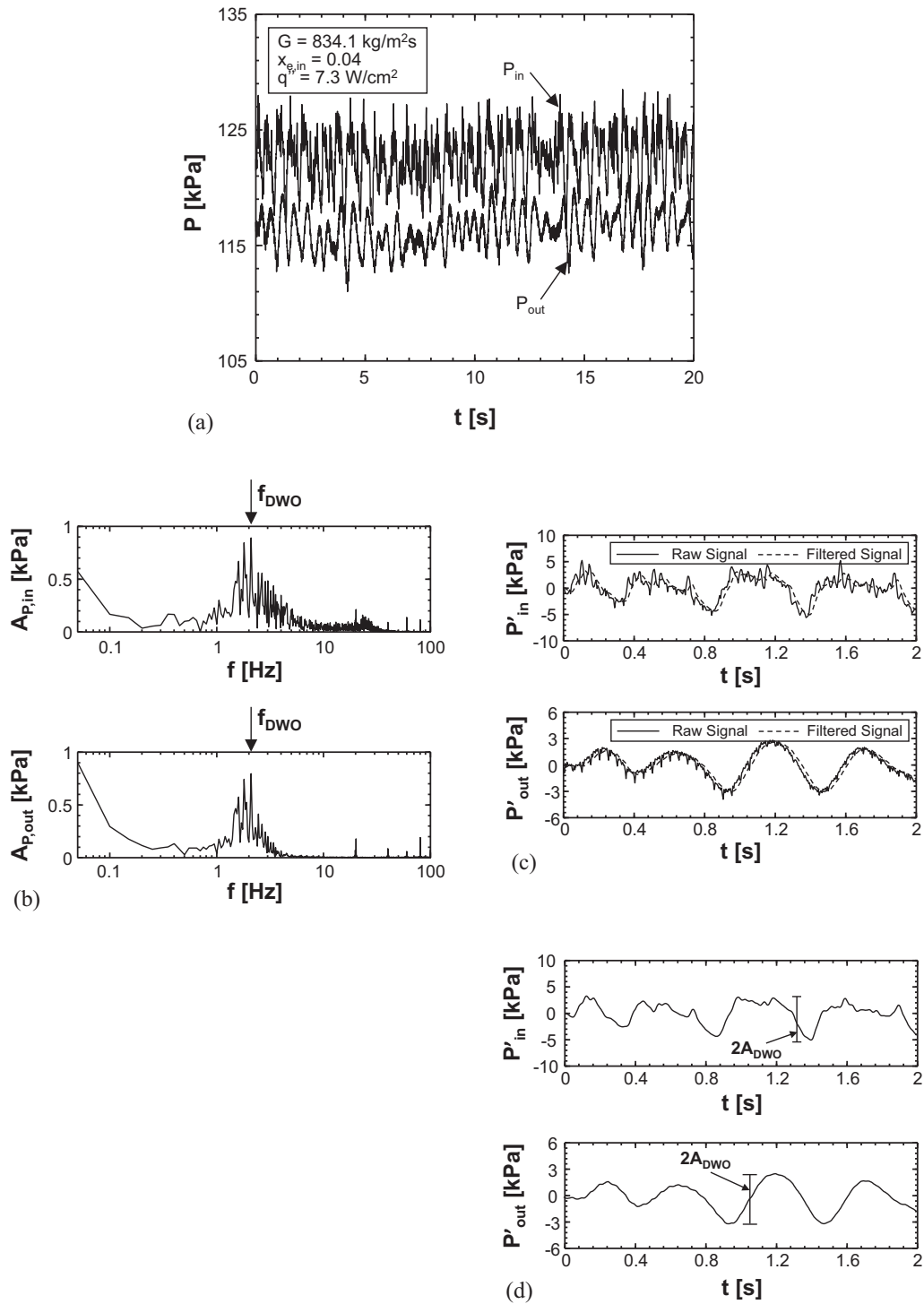


Fig. 8. Schematics outlining cyclical process behind DWOs, with (a) nominal conditions, (b) liquid accumulation in inlet region, (c) liquid slug/HDF advance, (d) HDF passage through heated length, and (e) return to nominal conditions.



**Fig. 9.** Plots showing detection methodology for DWO frequency and amplitude:(a) transient inlet and outlet pressure signals for entire fast Fourier transform (FFT) window, (b) associated FFTs with peak frequencies identified, (c) low-pass filtered pressure signals to isolate DWO behavior, and (d) DWO amplitude detection using filtered signals.

of smoothly continuous behavior associated with trigonometric functions (in other words, the derivatives of inlet pressure fluctuations would be closer to impulse functions than trigonometric functions). Outlet pressure fluctuations seem to exhibit behavior closer to sinusoidal, but are still not perfectly attributable to a single frequency and amplitude. Instead, these fluctuations can be best described using a Fourier series, or a linear combination of sine and cosine functions with associated amplitudes and

frequencies, all summing to a single curve within the time domain. The peak frequency detected in Fig. 9(b) is simply the frequency most closely associated (containing the most energy) with DWO induced oscillations.

Thus, alternate methodology must be employed to determine the amplitude at which DWO induced pressure fluctuations occur for a given set of operating conditions. To achieve this, fluctuating pressure  $P'$  is isolated, where

$$P' = P - P_{ave}, \quad (3)$$

and  $P$  and  $P_{ave}$  are the total and time-averaged pressures, respectively. Fig. 9(c) shows plots of fluctuating pressure versus time for both inlet and outlet pressures. The fluctuating pressures are plotted over a shortened period of 2 s to better highlight their structure. It is clear that both curves are composed of low-frequency fluctuations with high-frequency oscillations superimposed. This conclusion can also be drawn from analyzing amplitude versus frequency plots in Fig. 9(b), which show the majority of fluctuations occur in the 1–5 Hz range, but some sharp peaks may be detected in the 10–100 Hz range, likely attributable to mechanically induced oscillations [54]. To remove these high-frequency fluctuations and isolate the low frequency behavior attributable to DWOs, a second-order digital Butterworth low-pass filter with a cutoff frequency of 10 Hz is used, with the filter transfer function given by

$$H(z) = \frac{0.02 + 0.04z^{-1} + 0.02z^{-2}}{1.0 - 1.56z^{-1} + 0.64z^{-2}}. \quad (4)$$

Numerator and denominator coefficients are truncated here for presentation, but are output with additional significant figures by the python function used to generate them [92].

Filtered pressure fluctuations are identified with dashed lines in Fig. 9(c), and clearly illustrate that the high-frequency fluctuations have been removed. Careful analysis also reveals that there is a slight phase shift between the raw and filtered signals, which is characteristic of the filter type used here. This does not, however, impact the amplitude characteristics of the filtered signal.

Using the filtered pressure fluctuation curves, Fig. 9(d) illustrates how amplitude of oscillation can be determined by simply halving the difference between maximum and minimum values.

Moving forward, frequency and amplitude of oscillation for DWO induced behavior will be determined for both inlet and outlet pressure signals. These values will then be averaged to present a single characteristic DWO frequency and amplitude for each distinct set of operating conditions.

As discussed when analyzing Fig. 3, there can be slight differences in both amplitude and frequency of oscillation as detected at the inlet to the heated length versus the outlet. These differences are taken as being of minimal importance when compared to changes in frequency and amplitude with respect to changes in operating conditions, however, and it is these changes subsequent sections will aim to analyze.

#### 4.2. Frequency and amplitude of oscillation in response to changes in mass velocity, inlet quality, and heat flux

Fig. 10(a)–(d) presents plots of DWO frequency versus mass velocity for three different heat flux levels with  $x_{e,in} = 0.00$ – $0.04$ ,  $x_{e,in} = 0.07$ – $0.13$ ,  $x_{e,in} = 0.19$ – $0.25$ , and  $x_{e,in} = 0.30$ – $0.40$ , respectively, all gathered in year 1. Across all four plots, frequency of oscillation can be seen to increase with increasing mass velocity, indicating frequency of oscillation shares a direct relationship with flowrate. This is to be expected based on the current understanding of the phenomenon's manifestation, as the description provided along with Fig. 8 indicated momentum differences between the channel inlet, here represented by time-averaged mass velocity, and outlet (upstream and downstream of the HDF) are responsible for accelerating the HDF.

For similar reasons there are indications that, for some cases, increases in inlet quality lead to increases in frequency of oscillation. These increases can be attributed to flow acceleration due to increased void fraction leading to higher momentum fluxes (proportional to flow velocity squared), but, due to the fact that overall momentum is conserved for a single mass velocity at multiple qualities, this trend is secondary to that of mass velocity.

Changes in heat flux yield no discernable trend for frequency of oscillation, with each of the three heat flux levels shown exhibiting the peak frequency of oscillation for near-constant values of other operating conditions. This indicates phase change within the test module is of secondary importance to the hydrodynamic phenomenon at play, which is in line with the experimental observation of DWO induced behavior for cases with zero heat flux within the test section. It is likely, however, that phase change within the test section plays some role in the differences between inlet and outlet pressure signals as discussed in relation to Fig. 3.

Similarly, Fig. 11(a)–(d) present results for amplitude of DWO induced pressure oscillations versus mass velocity for three different heat flux levels with  $x_{e,in} = 0.00$ – $0.04$ ,  $x_{e,in} = 0.07$ – $0.13$ ,  $x_{e,in} = 0.19$ – $0.25$ , and  $x_{e,in} = 0.30$ – $0.40$ , respectively, also gathered in year 1. Across all subfigures, a similar trend of increasing amplitude with increasing mass velocity is present, indicating that both amplitude and frequency of oscillation are heavily tied to mass velocity. A slight increase in amplitude is also seen with increases in inlet quality, although it is of significantly lesser magnitude than that with respect to mass velocity, likely for the reasons mentioned when analyzing similar trends in Fig. 10.

Dissimilar to Fig. 10, however, is the dependence of amplitude of oscillation on heat flux, with the relative positions of three symbols denoting different heat flux levels indicating (for other operating conditions held nearly constant) higher amplitude oscillations are typically associated with higher values of heat flux. This can likely be attributed to boiling along the heated length during passage of high density fronts impacting the magnitude of pressure oscillations associated with DWOs.

Evident in both Figs. 10 and 11 is significant variability of results associated with the lowest mass velocity cases. This is likely due to the combined influence of three factors. First, the magnitude of oscillations is lowest for low mass velocity cases, meaning detection of DWO induced behavior becomes more difficult (other sources of fluctuations have a larger contribution to overall transient behavior). Second, all frequencies and amplitudes of oscillation in the present plots are determined using the methodology described in conjunction with Fig. 9 for transient pressure signals 20 s in duration. For the lowest mass velocity cases, which commonly exhibit frequencies of oscillation less than 1 Hz in magnitude, this means fewer samples with which to form an average for both frequency and amplitude of oscillation. Finally, for these low mass velocity cases, the ratio of inertia to body forces (commonly assessed using Froude number) is at its minimum, leading to the most irregular flow behavior of all cases analyzed here.

#### 4.3. Frequency and amplitude of oscillation in response to changes in relevant dimensionless groups

Prior to presenting results, it is necessary to define several relevant dimensionless groups as they will be used hereafter. Liquid Reynolds number,

$$Re_f = \frac{G(1 - x_{e,in})D_h}{\mu_f}, \quad (5)$$

where  $G$  is the mass velocity,  $x_{e,in}$  the thermodynamic equilibrium quality at the module inlet,  $D_h$  the hydraulic diameter, and  $\mu_f$  the liquid dynamic viscosity, is a mass fraction weighted ratio of inertial to viscous forces. Liquid Weber number,

$$We_f = \frac{\rho_f U_{char}^2 D_h}{\sigma}, \quad (6)$$

where  $\rho_f$  is the liquid density,  $\sigma$  the surface tension, and characteristic velocity  $U_{char}$  is defined as

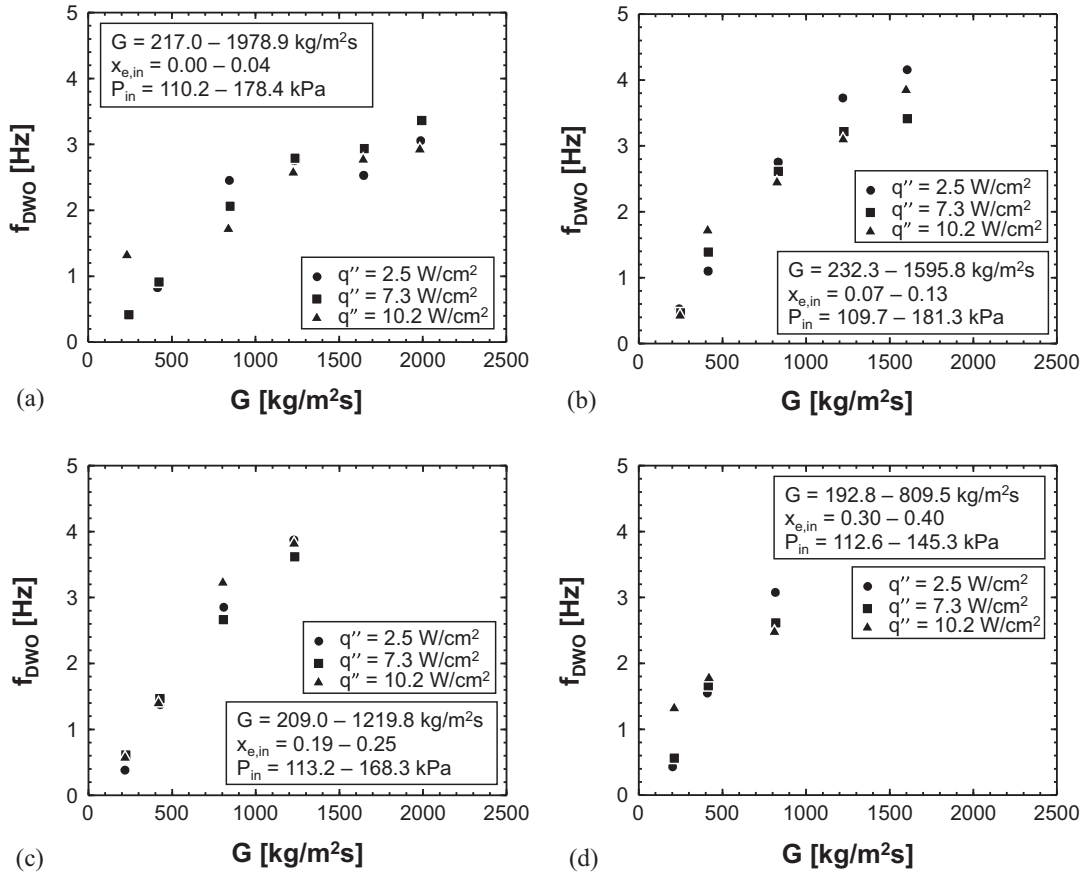


Fig. 10. Plots of DWO frequency versus mass velocity for three heat flux levels and (a)  $x_{e,in} = 0.00-0.04$ , (b)  $x_{e,in} = 0.07-0.13$ , (c)  $x_{e,in} = 0.19-0.25$ , and (d)  $x_{e,in} = 0.30-0.40$ .

$$U_{char} = \frac{G(1 - x_{e,in})}{\rho_f}, \quad (7)$$

providing a mass fraction weighted ratio of inertial to surface tension forces. Similarly, liquid Froude number,

$$Fr_f = \frac{\frac{G}{\rho_f}(1 - x_{e,in})}{\sqrt{gD_h}}, \quad (8)$$

represents a mass fraction weighted ratio of inertia to body forces. It should be noted that these first three dimensionless groups in Eqs. (5), (6) and (8) all contain flow inertia terms in their numerators, and denominators that exhibit little to no change for the current operating conditions ( $\mu_f$  and  $\sigma$  change slightly with operating pressure, while  $g$  and  $D_h$  remain constant).

The final two dimensionless groups, boiling number,  $Bo$ , and phase change number,  $N_{pch}$ , contain both numerators and denominators that change continuously across operating conditions, and provide measures of the relative magnitudes of phase change processes to flow inertia, with phase change number being weighted by phase density differences. Here, they are defined as

$$Bo = \frac{q''}{Gh_{fg}} \quad (9)$$

and

$$N_{pch} = \frac{Q}{\dot{m}h_{fg}} \frac{v_g - v_f}{v_f}, \quad (10)$$

where  $q''$  is the heat flux,  $h_{fg}$  the latent heat of vaporization,  $Q$  the total energy added within FBM,  $\dot{m}$  the mass flowrate, and  $v_g$  and  $v_f$  the vapor and liquid specific volumes, respectively.

Fig. 12(a)–(e) shows trends for DWO frequency versus each of the respective dimensionless groups mentioned above. It should be noted that data from both 2015 and 2016 experiments are present on these plots, allowing for comparison of data across the two sets of experiments for similar values of the relevant dimensionless groups. Data acquired in 2015 are denoted with circles and those from 2016 with squares.

Fig. 12(a) shows that, as liquid Reynolds number increases, there is a clear increase in frequency of oscillation for DWO induced pressure fluctuations. This matches well with the trend of increasing frequency with increasing mass velocity seen in Fig. 10, as mass velocity is present in the numerator of Eq. (5). Frequency values appear to plateau, however, for values of liquid Reynolds number greater than  $\sim 10000$ , indicating some physical limits for frequency at which this phenomenon can occur for the present flow geometry and working fluid.

Similarly, Fig. 12(b) and (c) show increases in frequency for increases in liquid Weber and Froude numbers, respectively, with both also exhibiting diminishing returns past some moderate value. This indicates flow inertia is by far the dominant force at play relative to other hydrodynamic effects.

Fig. 12(d) and (e), providing plots of frequency versus boiling and phase change numbers, respectively, exhibit no clear trends with respect to these dimensionless groups. If anything, Fig. 12(d) exhibits a slight negative trend, indicating mass velocity (present in the denominator of Eq. (9)) continues to the frequency at which DWOs occur. This further reinforces the trend seen in Fig. 10, that heat flux level (and the phase change process in general) has little effect on the frequency at which DWOs occur.

Fig. 13(a)–(e) provides similar plots for amplitude of DWO induced oscillations versus relevant dimensionless groups. Similar

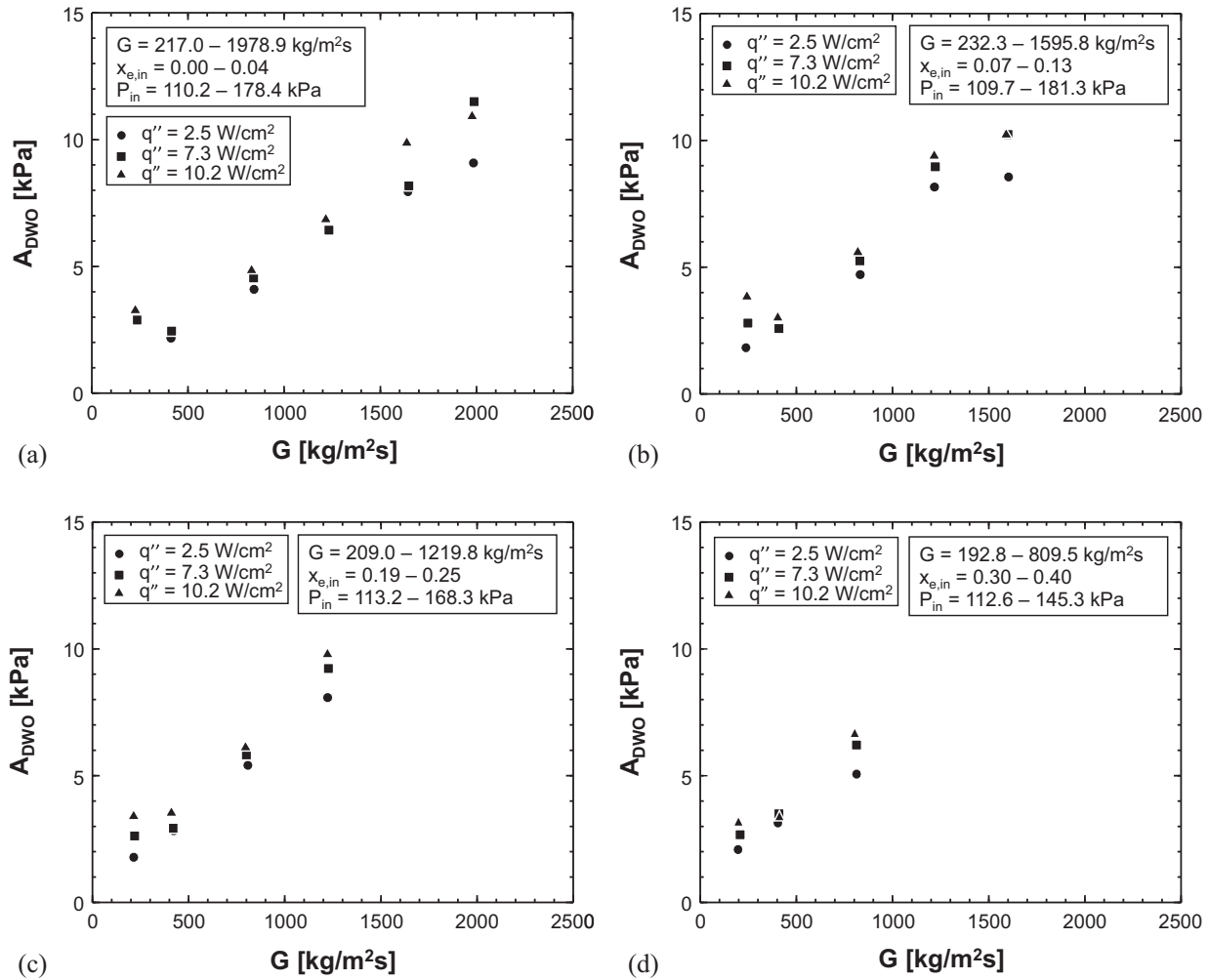


Fig. 11. Plots of DWO amplitude versus mass velocity for three heat flux levels and (a)  $x_{e,in} = 0.00-0.04$ , (b)  $x_{e,in} = 0.07-0.13$ , (c)  $x_{e,in} = 0.19-0.25$ , and (d)  $x_{e,in} = 0.30-0.40$ .

to the counterparts in Fig. 12(a)–(c), plots of amplitude versus liquid Reynolds, Weber, and Froude numbers exhibit strong positive trends. They also show signs of plateauing in the higher portion of the range for each dimensionless group, but without quite as strong a change in slope, indicating the mechanism(s) limiting frequency of oscillation are also present for amplitude, but without quite as strong an impact.

Fig. 13(d) and (e) shows plots of amplitude versus boiling and phase change numbers, respectively; neither of which exhibit strong trends. This is somewhat surprising, as Fig. 11 clearly showed increases in amplitude of oscillation associated with increases in heat flux, but can likely be explained by the competing influences of phase change (numerator) and flow inertia (denominator) of both dimensionless groups. If anything, slight negative trends are present within these plots, indicating the influence of flow inertia is still the dominant factor here.

Across both Figs. 12 and 13, it can be seen that frequency and amplitude results from experiments conducted in both year 1 and year 2 of the project show good agreement, with few outliers. This reinforces the idea presented in prior work by the present authors [54], that DWO induced oscillatory flow behavior within the test section can be isolated from other fluctuations, and it occurs largely independent of other hardware within the flow loop, validating it as a physical phenomenon intrinsic to two-phase flows.

#### 4.4. Coupling of frequency and amplitude of oscillation

In analyzing Figs. 10–13, it is clear that both frequency and amplitude of DWO induced oscillatory behavior depend primarily on flow inertia. This is in keeping with the DWO process presented schematically in Fig. 8, in which flow inertia is directly responsible for advecting the HDF along the channel length.

Fig. 14, providing a plot of DWO amplitude versus frequency, further reinforces this notion by illustrating the nearly-linear relationship between the two key aspects of DWO behavior. The importance of this in validating physicality of the aforementioned DWO process schematic cannot be understated, and looking forward, coupling of frequency and amplitude of DWO induced oscillatory behavior is a requirement for any predictive tools attempting to predict these key characteristics of DWOs.

It is also worth noting that, across all operating conditions evaluated in this section, the amplitude of pressure fluctuations as a percentage of time-averaged operating pressure is of sufficiently low magnitude (at most 7%) to alleviate any concerns of them posing safety risks to system operation (especially important for development of the FBCE). Magnitudes are sufficient, however, to potentially trigger pre-mature CHF, dryout, or choked flow should operating conditions place a system sufficiently close to these critical points, a concern which should be kept in mind for design of two-phase flow thermal management systems.

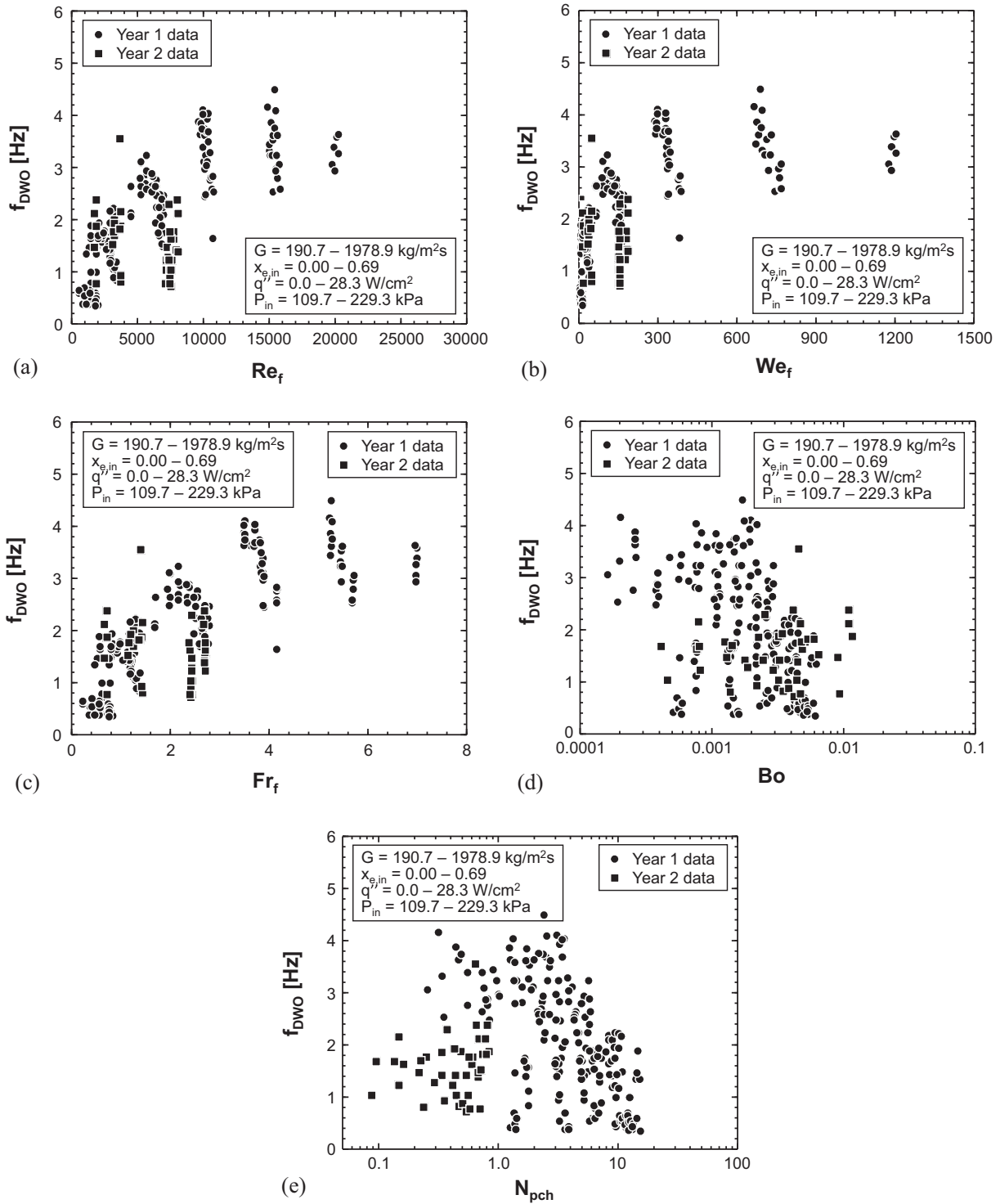


**Fig. 12.** Plots of DWO frequency versus (a) liquid Reynolds number,  $Re_f$ , (b) liquid Weber number,  $We_f$ , (c) liquid Froude number,  $Fr_f$ , (d) boiling number,  $Bo$ , and (e) phase change number,  $N_{pch}$ .

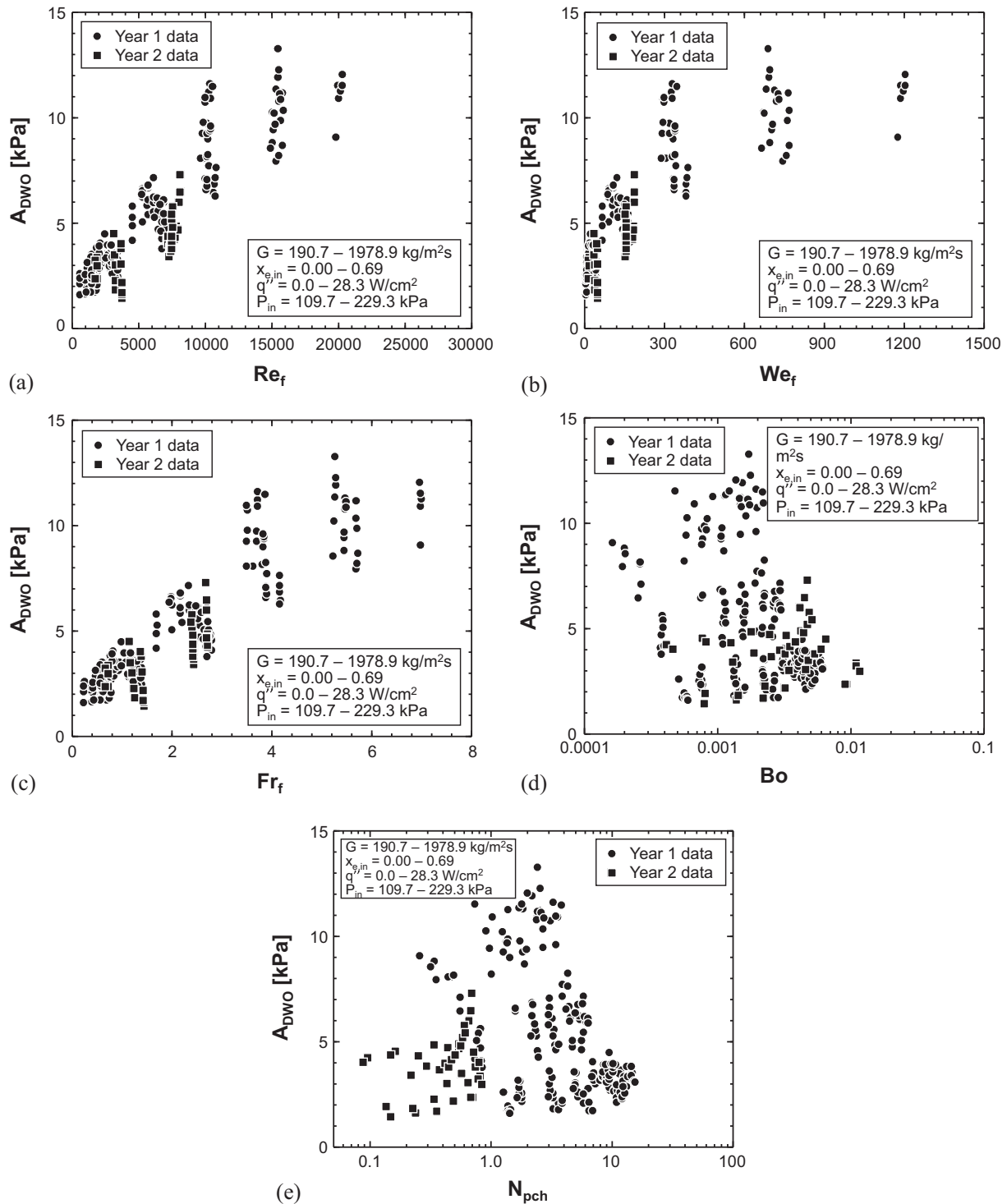
## 5. Utilizing frequency and amplitude information

### 5.1. Reconstruction of experimental pressure fluctuations

Having presented flow visualization images and schematics outlining the process by which density wave oscillations occur in mini/macro-channels and analyzed a large experimental database of 236 cases for vertical upflow boiling with DWOs present to

gather information on trends, some discussion on utility of gathered data is warranted.

Thus far, all discussion on DWOs has centered on frequency and amplitude of induced oscillatory behavior. As discussed with Fig. 9, however, DWOs do not exhibit perfectly sinusoidal behavior, meaning any reconstruction of DWO induced behavior using a single frequency and amplitude is by nature an approximation.



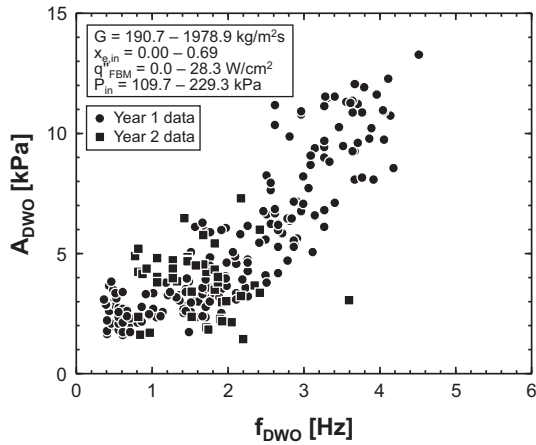
**Fig. 13.** Plots of DWO amplitude versus (a) liquid Reynolds number,  $Re_f$ , (b) liquid Weber number,  $We_f$ , (c) liquid Froude number,  $Fr_f$ , (d) boiling number,  $Bo$ , and (e) phase change number,  $N_{pch}$ .

Fig. 15(a)–(e) investigates the potential accuracy of such a reconstruction, using inlet pressure signal for the case with mass velocity of  $G = 834.1 \text{ kg/m}^2 \text{ s}$ , inlet quality of  $x_{e,in} = 0.04$ , average inlet pressure of  $P_{in} = 122.6 \text{ kPa}$ , and heat flux of  $q'' = 7.3 \text{ W/cm}^2$ . Fig. 15(a) shows the fluctuating pressure signal as well as the reconstructed signal, defined as

$$P'_{rec} = A_{DWO,in} \sin(2\pi f_{DWO,in} t), \quad (11)$$

where  $A_{DWO,in}$  and  $f_{DWO,in}$  are the amplitude and frequency of DWO induced oscillatory behavior detected for the inlet pressure signal using the methodology presented in Fig. 9, and  $t$  is time.

It is clear from Fig. 15(a) that the reconstructed signal does a reasonable job of approximating the original signal. A key limitation, however, is the slow change in phase between the two waveforms over time. At the first trough of the waveforms, the reconstructed signal is slightly ahead of the experimental data,



**Fig. 14.** Plot of DWO amplitude versus frequency for all data from years 1 and 2 of the study.

but at the second trough they exhibit an almost exact match. The third trough shows the reconstructed signal lagging slightly behind the experimental data and, by the end of the 2-s window shown

here, the two waveforms appear to be 180° out of phase. This is again due to the features of DWOs discussed in Fig. 9, specifically that DWO induced behavior is not perfectly sinusoidal in nature and the frequency at which DWOs occur is not constant, falling instead within a narrow range.

For comparison purposes, Fig. 15(b)–(e) provides similar plots of experimental fluctuating pressure alongside 2nd, 3rd, 4th, and 8th order Fourier series expansions, respectively. These Fourier series expansions are of the form

$$P'_{FourierSeries} = \frac{a_0}{2} + \sum_{k=1}^n (a_k \cos(kt) + b_k \sin(kt)), \quad (12)$$

where  $n$  is the series order and coefficients  $a$  and  $b$  are determined in Matlab [93]. From these plots it can be qualitatively seen that the reconstructed signal shown in Fig. 15(a) and expressed in Eq. (11) is superior to the 2nd order series expansion, of comparable accuracy to 3rd and 4th order series, but significantly inferior to the 8th order series for the current window of analysis.

More rigorous evaluation of the agreement between waveforms can be assessed by computing cross correlation coefficients for each respective original and reconstructed signal. The cross

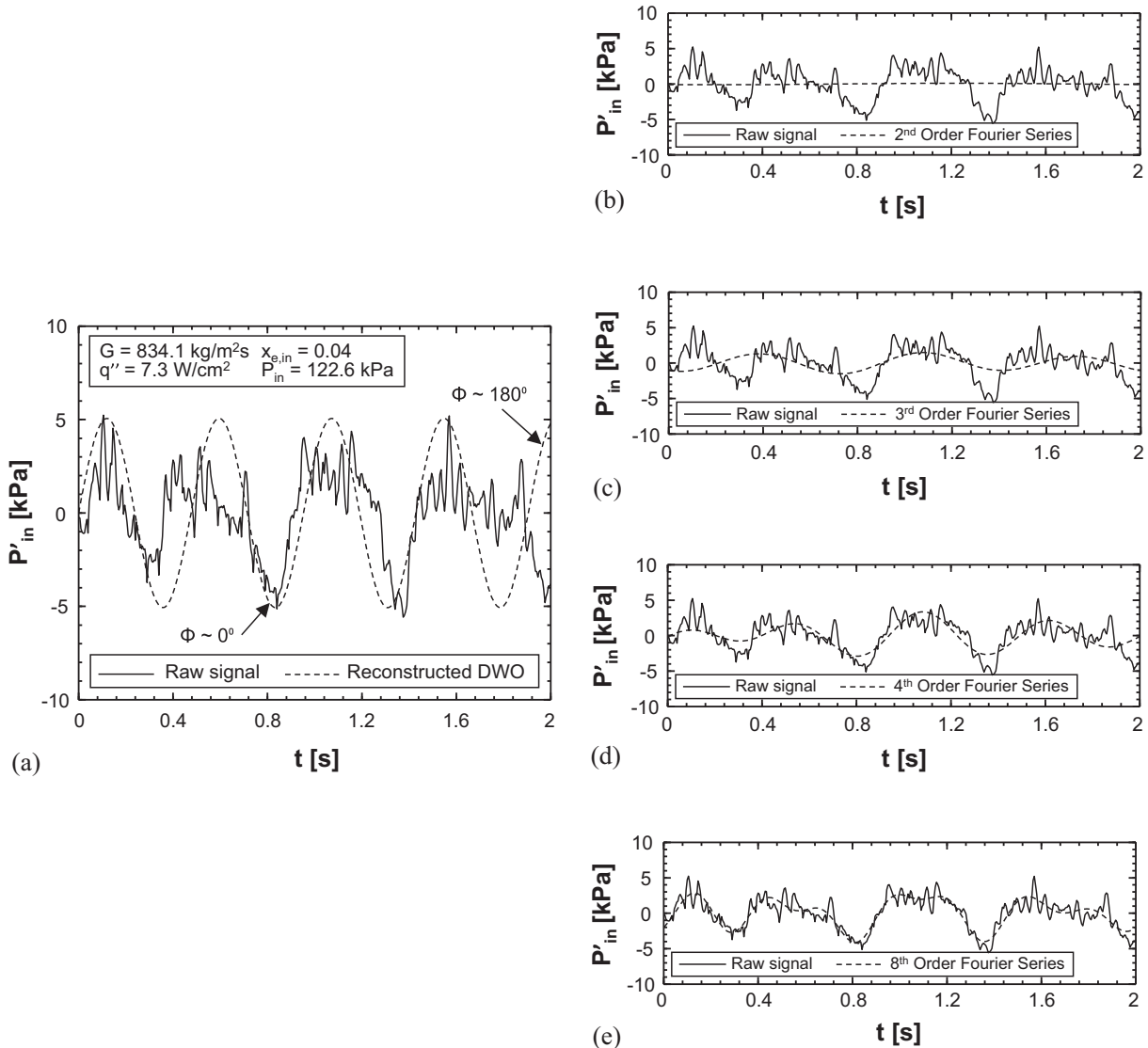


**Fig. 15.** Plots of FBM heated length inlet pressure fluctuations along with (a) curve reconstructed from DWO amplitude and frequency, (b) 2nd order Fourier series expansion, (c) 3rd order Fourier series expansion, (d) 4th order Fourier series expansion, and (e) 8th order Fourier series expansion.

correlation coefficient provides a measure of similarity between two waveforms, and is defined as

$$\rho_{cc}(P'_{exp}, P'_{rec}) = \frac{1}{N-1} \sum_{i=1}^N \left[ \left( \frac{P'_{exp,i} - \mu_{P'_{exp}}}{\sigma_{P'_{exp}}} \right) \left( \frac{P'_{rec,i} - \mu_{P'_{rec}}}{\sigma_{P'_{rec}}} \right) \right], \quad (13)$$

where  $P'_{exp}$  and  $P'_{rec}$  are the experimental and reconstructed fluctuating pressures,  $N$  is the number of samples in each waveform, and  $\mu$  and  $\sigma$  refer to respective means and standard deviations. Values fall in the range  $[-1,1]$ , where 1 represents exact match, -1 indicates 180° phase difference, and 0 indicates no correlation between waveforms. It is also possible to think of the cross correlation coefficient as the covariance of the two waveforms divided by the multiplication of their standard deviations, or

$$\rho_{cc}(P'_{exp}, P'_{rec}) = \frac{\text{cov}(P'_{exp}, P'_{rec})}{\sigma_{P'_{exp}} \sigma_{P'_{rec}}}. \quad (14)$$

Table 2 provides values of cross correlation coefficient for each of the waveform pairs shown in Fig. 15(a)–(e). From these values it is clear that the reconstruction provided in Fig. 15(a) is superior to 2nd and 3rd order Fourier series expansions, but inferior to 4th and 8th order expansions.

It should be noted here that the cross correlation coefficient does exhibit some dependence on the time period over which the reconstruction is evaluated, especially for very short periods where phase between the two waveforms plays a vital role. Over longer periods these errors average out, and cross correlation coefficients for waveforms reconstructed using experimental amplitude and frequency provide more representative values. Towards this end, Table 3 provides values of cross correlation coefficient evaluated on the same 20-s period used for frequency and amplitude detection.

Table 3 contains values of cross correlation coefficient  $\rho_{cc}$  evaluated using waveforms reconstructed using information from inlet and outlet oscillations separately as well as averaged values. It can be seen that across the four sets of operating conditions presented herein, cases with similar values for frequency and amplitude of inlet and outlet pressure fluctuations, respectively, yield little difference in reconstruction accuracy when evaluated using local (inlet and outlet) information versus averaged information. However, for the two cases presented here with significant difference between inlet and outlet values of frequency, reconstruction accuracy appears to be significantly different for the two methods of evaluation.

**Table 2**  
Cross correlation coefficients for waveform pairs in Fig. 15.

Original signal	Reconstruction	Period for evaluation [s]	Cross correlation coefficient, $\rho_{cc}$
Experimental inlet fluctuating pressure	2nd order Fourier series expansion	2	0.10
Experimental inlet fluctuating pressure	3rd order Fourier series expansion	2	0.40
<b>Experimental inlet fluctuating pressure</b>	<b>Experimentally detected frequency and amplitude</b>	2	<b>0.48</b>
Experimental inlet fluctuating pressure	4th order Fourier series expansion	2	0.71
Experimental inlet fluctuating pressure	8th order Fourier series expansion	2	0.87

Overall, it appears accuracy of reconstruction is far more sensitive to frequency than amplitude. This makes sense, as differences in phase cause multiplicative errors when evaluating the sum in Eq. (13), while differences in amplitude only cause additive errors.

Information provided in Table 3 indicates values of cross-correlation coefficient for the present reconstruction method fall predominantly in the  $-0.40$  to  $0.40$  range. This indicates a reasonable degree of fit for the reconstruction method, with major information regarding amplitude and frequency of oscillation captured, but simplifications limiting its ability to fully reconstruct the complex transient waveform. The primary limiting assumptions are:

- (1) DWO induced flow oscillations are perfectly sinusoidal in nature, which has been shown not to be very accurate.
- (2) DWOs occur at constant frequency and amplitude, which has also been shown not to be very accurate.
- (3) The contribution of other induced fluctuations (whether high frequency, mechanically induced phenomena, or low frequency system transients) are negligible to overall system dynamic behavior, which cannot be assumed universally true.

Without addressing these limitations, it is unlikely higher accuracy reconstructions can be performed.

Accuracy of reconstruction is not the key benefit of this method of decomposing DWO induced behavior into single frequency and amplitude, however. Rather, it is the ability to utilize this information to easily characterize DWO induced fluctuations and implement them as boundary conditions and/or model inputs for fully transient two-phase flow simulations.

## 5.2. Key trends/outcomes useful for future model development

Although a key aspect of two-phase flow research for decades (with the first work in the field commonly attributed to Serov [48]), an easily utilized, unified method for dealing with the impact of DWO induced flow oscillations in phase-change thermal management systems is still lacking.

As mentioned in Section 3.1, many classic studies adopted approaches based on classic stability theory, modeling information propagation within the boiling section of the flow loop to determine unstable conditions for which DWOs would be encountered during subcooled boiling. Studies such as those by Fukuda and Kobori [94] and Lahey and Podowski [47] based their analysis on experimentally observed phenomena and demonstrated some qualitative agreement between stability boundary model and results, but little focus was spent on verifying agreement between experimental and predicted amplitude and frequency of oscillation. Additionally, that their analysis centered on subcooled flow boiling indicates a different forcing function was present for DWOs in their systems compared to that analyzed in the present work, limiting the applicability of their analysis to the current configuration.

More recent work by Schlichting et al. [62] accounted for the presence of instability-induced fluctuations within their system model by introducing mass flowrate fluctuations of a specified magnitude. Another study by Alves et al. [95] introduced transient phenomena within their analytic model by using transient experimental inlet pressure as a boundary condition. While both studies provide comprehensive analytical models for transient two-phase flow behavior, the lack of a physical constitutive relationship for DWO (or other instability modes) induced oscillatory behavior is a key limitation hindering the utility of their respective models to act as purely predictive design tools.

Development and validation of a model to predict frequency and amplitude of DWO induced fluctuations would prove a

**Table 3**

Cross correlation coefficients for inlet and outlet pressure fluctuations under various operating conditions.

Original signal	Operating conditions	Detected freq. [Hz]	Detected amp. [kPa]	Average freq. [Hz]	Average amp. [kPa]	Period for evaluation [s]	$\rho_{cc}$ (individual)	$\rho_{cc}$ (average)
$P'_{in}$	$G = 834.1 \text{ kg/m}^2\text{s}$	2.1	5.1	2.1	4.6	20	0.24	0.24
$P'_{out}$	$x_{e,in} = 0.04$ $P_{in,ave} = 122.6 \text{ kPa}$ $q'' = 7.3 \text{ W/cm}^2$	2.1	4.1			20	-0.28	-0.28
$P'_{in}$	$G = 1636.5 \text{ kg/m}^2\text{s}$	3.8	9.6	3.0	8.2	20	0.14	-0.002
$P'_{out}$	$x_{e,in} = 0.01$ $P_{in,ave} = 154.6 \text{ kPa}$ $q'' = 7.3 \text{ W/cm}^2$	2.2	6.9			20	-0.35	-0.11
$P'_{in}$	$G = 407.8 \text{ kg/m}^2\text{s}$	0.95	2.8	0.95	2.5	20	-0.33	-0.33
$P'_{out}$	$x_{e,in} = 0.03$ $P_{in,ave} = 116.0 \text{ kPa}$ $q'' = 7.3 \text{ W/cm}^2$	0.95	2.3			20	-0.14	-0.14
$P'_{in}$	$G = 816.1 \text{ kg/m}^2\text{s}$	3.1	6.6	2.5	5.6	20	-0.20	-0.04
$P'_{out}$	$x_{e,in} = 0.11$ $P_{in,ave} = 130.5 \text{ kPa}$ $q'' = 10.2 \text{ W/cm}^2$	1.9	4.6			20	0.08	0.15

**Table 4**

Key findings from the present study.

Aspect of study	Key findings
Manifestation of DWOs	<ul style="list-style-type: none"> <li>Unlike micro-channels, where surface tension forces are integral in the formation and propagation of DWOs, DWOs in mini/macro-channel flows with finite inlet quality manifest due to flow separation effects</li> <li>Manifestation of DWOs in the present geometry is due to a cyclical process of upstream liquid film accumulation and downstream dryout, leading to mass and momentum flux imbalances between channel inlet and outlet, which cause formation and propagation of a liquid slug (HDF) along the channel, re-wetting walls and re-establishing co-current annular flow</li> </ul>
Frequency of induced oscillations	<ul style="list-style-type: none"> <li>Average frequency of DWO induced oscillations depends primarily on mass velocity and shows little dependence on heat flux</li> <li>Frequency of pressure oscillations occasionally differs between measurement locations upstream and downstream of the heated length, likely due to phase change processes taking place within altering flow characteristics</li> <li>DWOs are periodic but not necessarily sinusoidal in nature</li> <li>DWOs do not occur at a single constant frequency, with oscillatory behavior instead falling in a narrow frequency band around a peak value</li> </ul>
Amplitude of induced pressure oscillations	<ul style="list-style-type: none"> <li>Amplitude of DWO induced pressure oscillations depends primarily on mass velocity, with a lesser dependence on heat flux along the heated length</li> <li>Amplitude of DWO induced pressure oscillations also differs slightly between measurement locations upstream and downstream of the heated length, likely due to phase change processes taking place within altering flow characteristics</li> </ul>
Reconstruction of experimental pressure signals using frequency and amplitude	<ul style="list-style-type: none"> <li>Reconstruction using peak frequency and average amplitude of oscillation exhibits acceptable agreement when evaluating cross correlation coefficients</li> <li>Disagreement stems from (1) continuously changing phase lag between waveforms due to oversimplification associated with using single frequency, and (2) reconstruction lacking high and low frequency information</li> <li>Despite limitations, reconstruction is considered more than adequate for use as boundary condition to propagate DWO induced fluctuations into transient two-phase flow models</li> </ul>

valuable constitutive relationship for transient two-phase flow codes due to its ability to more realistically simulate variations in operating pressure and flowrate which then impact important design parameters such as heated wall temperature, heat transfer coefficient, and CHF value through both direct means (e.g., changes to local flow field) and indirect means (e.g., changes to thermo-physical properties). Despite the use of a single frequency and amplitude to reconstruct transient experimental results exhibiting less-than-perfect agreement, a tool capable of predicting peak frequency and amplitude of DWO induced fluctuations would prove a major step forward towards the ability to design around such oscillatory behavior.

Towards this end, the companion work to the present study [88] aims to present a new mechanistic model for DWOs capable of predicting frequency of induced oscillatory behavior as well as amplitude of associated pressure fluctuations. This work will draw heavily from key conclusions drawn from analyzing the experimental results presented herein, which are summarized in Table 4.

## 6. Conclusions

This study investigated mechanisms behind the occurrence of Density Wave Oscillations (DWOs) and the characteristics of these oscillations in vertical upflow boiling of FC-72 within a single mini-channel. Based on conclusions from prior studies by the present authors [53,54], only conditions for which DWOs were observed within the test module were analyzed, providing a total of 236 data points spanning two separate sets of testing. Sequences of flow visualization images were presented to provide a mechanistic understanding of the DWO process, followed by schematics detailing this information. A methodology for detecting frequency and amplitude of oscillation was detailed and utilized to provide information regarding trends for frequency and amplitude of DWO induced pressure oscillations with respect to key operating parameters such as mass velocity, inlet quality, and heat flux, as well as relevant dimensionless groups. Some analysis regarding the validity of reconstructing transient pressure signals using a single frequency and amplitude was also included, along with discussion

on the utility of a predictive tool capable of determining frequency and amplitude for given operating conditions. Key findings from this study are as follows:

- (1) Analysis of flow visualization results reveals the dominant, low-frequency oscillatory mode within the current system can be related to the cyclical passage of high and low density fronts through the test module, a process itself attributable to flow separation effects.
- (2) Trends for frequency and amplitude of oscillation remain consistent across the two sets of experiments presented herein, and indicate mass velocity is the dominant factor in determining both frequency and amplitude of DWO induced pressure oscillations.
- (3) DWO induced pressure oscillation amplitude was seen to be at most 7% of time-averaged inlet pressure, indicating there is little safety risk associated with the present operating conditions (important for FBCE operation on the ISS).
- (4) Reconstruction of transient pressure fluctuations using a single frequency and amplitude yielded moderate agreement with original transient waveforms, with key limitations being the insufficiency of a single frequency to describe DWO induced behavior and lost low and high frequency information.
- (5) Although imperfect for recreating experimental pressure results, a predictive model for frequency and amplitude of DWO induced fluctuations capable of serving as a constitutive relationship for advanced transient two-phase flow simulations would prove valuable.

## Acknowledgements

The authors are grateful for financial support provided by the National Aeronautics and Space Administration (NASA) under grant no. NNX17AK98G, and technical support of the NASA Glenn Research Center, Cleveland, Ohio. This work was also supported by NASA Space Technology Research Fellowship NNX15AP29H. The authors would also like to thank Chirag Kharangate and Aubrey Lokey for assistance gathering experimental data presented here.

## Conflict of interests

None declared.

## Appendix A. Supplementary material

Supplementary data associated with this article can be found, in the online version, at <https://doi.org/10.1016/j.ijheatmasstransfer.2018.04.138>.

## References

- [1] I. Mudawar, Assessment of high-heat-flux thermal management schemes, *IEEE Trans. - CPMT* 24 (2001) 122–141.
- [2] C.L. Tien, K.S. Chung, Entrainment limits in heat pipes, *AIAA J.* 17 (1979) 643–646.
- [3] T.J. LaClair, I. Mudawar, Thermal transients in a capillary evaporator prior to the initiation of boiling, *Int. J. Heat Mass Transfer* 43 (2000) 3937–3952.
- [4] M. Shafahi, V. Bianco, H. Vafai, O. Manco, An investigation of the thermal performance of cylindrical heat pipes using nanofluids, *Int. J. Heat Mass Transfer* 53 (2010) 376–383.
- [5] P.J. Marto, V.J. Lepere, Pool boiling heat transfer from enhanced surfaces to dielectric fluids, *J. Heat Transfer* 104 (1982) 292–299.
- [6] I. Mudawar, T.M. Anderson, Parametric investigation into the effects of pressure, subcooling, surface augmentation and choice of coolant on pool boiling in the design of cooling systems for high-power density chips, *J. Electronic Packaging* 112 (1990) 375–382.
- [7] I. Mudawar, T.M. Anderson, Optimization of extended surfaces for high flux chip cooling by pool boiling, *J. Electronic Packaging* 115 (1993) 89–100.
- [8] J.A. Shmerler, I. Mudawar, Local heat transfer coefficient in wavy free-falling turbulent liquid films undergoing uniform sensible heating, *Int. J. Heat Mass Transfer* 31 (1988) 67–77.
- [9] I. Mudawar, R.A. Houpt, R.A., Mass and momentum transport in smooth falling liquid films laminarized at relatively high Reynolds numbers, *Int. J. Heat Mass Transfer* 36 (1993) 3437–3448.
- [10] C.O. Gersey, I. Mudawar, Effects of heater length and orientation on the trigger mechanism for near-saturated flow boiling CHF - I. Photographic and statistical characterization of the near-wall interfacial features, *Int. J. Heat Mass Transfer* 38 (1995) 629–642.
- [11] S.M. Ghiaasiaan, *Two-phase Flow, Boiling and Condensation in Conventional and Miniature Systems*, Cambridge University Press, New York, 2008.
- [12] W. Qu, I. Mudawar, Thermal design methodology for high-heat-flux single-phase and two-phase micro-channel heat sinks, in: *Proc. I-THERM 2002*, San Diego, California, pp. 347–359.
- [13] S. Mukherjee, I. Mudawar, Smart pumpless loop for micro-channel electronic cooling using flat and enhanced surfaces, *IEEE Trans. - CPMT* 26 (2003) 99–109.
- [14] S. Mukherjee, I. Mudawar, Pumpless loop for narrow channel and micro-channel boiling from vertical surfaces, *J. Electronic Packaging* 125 (2003) 431–441.
- [15] J. Lee, I. Mudawar, Critical heat flux for subcooled flow boiling in micro-channel heat sinks, *Int. J. Heat Mass Transfer* 52 (2009) 3341–3352.
- [16] J. Lee, I. Mudawar, Fluid flow and heat transfer characteristics of low temperature two-phase micro-channel heat sinks - part 1: Experimental methods and flow visualization results, *Int. J. Heat Mass Transfer* 51 (2008) 4315–4326.
- [17] M. Monde, T. Inoue, Critical heat flux in saturated forced convective boiling on a heated disk with multiple impinging jets, *J. Heat Transfer* 113 (1991) 722–727.
- [18] D.C. Wadsworth, I. Mudawar, Enhancement of single-phase heat transfer and critical heat flux from an ultra-high-flux simulated microelectronic heat source to a rectangular impinging jet of dielectric liquid, *J. Heat Transfer* 114 (1992) 764–768.
- [19] M.E. Johns, I. Mudawar, An ultra-high power two-phase jet-impingement avionic clamshell module, *J. Electronic Packaging* 118 (1996) 264–270.
- [20] I. Mudawar, Recent advances in high-flux, two-phase thermal management, *J. Thermal Sci. Eng. Appl.* 5 (2013) 021012.
- [21] W.P. Klinzing, J.C. Rozzi, I. Mudawar, Film and transition boiling correlations for quenching of hot surfaces with water sprays, *J. Heat Treating* 9 (1992) 91–103.
- [22] D.D. Hall, I. Mudawar, Experimental and numerical study of quenching complex-shaped metallic alloys with multiple, overlapping sprays, *Int. J. Heat Mass Transfer* 38 (1995) 1201–1216.
- [23] L. Lin, R. Ponnappan, Heat transfer characteristics of spray cooling in a closed loop, *Int. J. Heat Mass Transfer* 46 (2003) 3737–3746.
- [24] J.D. Bernardin, I. Mudawar, A Leidenfrost point model for impinging droplets and sprays, *J. Heat Transfer* 126 (2004) 272–278.
- [25] M. Visaria, I. Mudawar, Effects of high subcooling on two-phase spray cooling and critical heat flux, *Int. J. Heat Mass Transfer* 51 (2008) 5269–5278.
- [26] I. Mudawar, D. Bharathan, K. Kelly, S. Narumanchi, Two-phase spray cooling of hybrid vehicle electronics, *IEEE Trans. - CPMT* 32 (2009) 501–512.
- [27] M. Visaria, I. Mudawar, Application of two-phase spray cooling for thermal management of electronic devices, *IEEE Trans. - CPMT* 32 (2009) 784–793.
- [28] I. Mudawar, Two-phase micro-channel heat sinks: theory, applications and limitations, *J. Electronic Packaging* 133 (2011), 041002-2.
- [29] M.K. Sung, I. Mudawar, Experimental and numerical investigation of single-phase heat transfer using a hybrid jet impingement/micro-channel cooling scheme, *Int. J. Heat Mass Transfer* 49 (2006) 682–694.
- [30] M.K. Sung, I. Mudawar, Single-phase hybrid micro-channel/jet impingement cooling, *Int. J. Heat Mass Transfer* 51 (2008) 4342–4352.
- [31] M.K. Sung, I. Mudawar, Single-phase and two-phase heat transfer characteristics of low temperature hybrid micro-channel/micro-jet impingement cooling module, *Int. J. Heat Mass Transfer* 51 (2008) 3882–3895.
- [32] S. Lee, I. Mudawar, M.M. Hasan, Thermal analysis of hybrid single-phase, two-phase and heat pump thermal control system (TCS) for future spacecraft, *Appl. Therm. Eng.* 100 (2016) 190–214.
- [33] F.P. Chiramoto, J.A. Joshi, Workshop on critical issues in microgravity fluids, transport, and reaction processes in advanced human support technology - final report, NASA TM-2004-212940, 2004.
- [34] The National Academies, *Recapturing a Future for Space Exploration: Life and Physical Sciences Research for a New Era*, National Academies Press, Washington, DC, 2011.
- [35] H. Zhang, I. Mudawar, M.M. Hasan, Flow boiling CHF in microgravity, *Int. J. Heat Mass Transfer* 48 (2005) 3107–3118.
- [36] H. Zhang, I. Mudawar, M.M. Hasan, Application of flow boiling for thermal management of electronics in microgravity and reduce-gravity space systems, *IEEE Trans. - CPMT: Components Packaging Technol.* 32 (2009) 466–477.
- [37] M. Ishii, N. Zuber, Thermally induced instabilities in two-phase mixtures, in: *Proc. 4th Int. Heat Transfer conf. on Heat Transfer* (1970), Paris, vol. 5, paper B5.11.
- [38] D. Brutin, L. Tadrist, Pressure drop and heat transfer analysis of flow boiling in a minichannel: influence of the inlet condition on two-phase flow stability, *Int. J. Heat Mass Transfer* 47 (2004) 2365–2377.

- [39] G. Wang, P. Cheng, A.E. Bergles, Effects of inlet/outlet configurations on flow boiling instability in parallel microchannels, *Int. J. Heat Mass Transfer* 51 (2008) 2267–2281.
- [40] R.H. Whittle, R. Forgan, A correlation for the minima in the pressure drop versus flow-rate curves for sub-cooled water flowing in narrow heated channels, *Nucl. Eng. Des.* 6 (1967) 89–99.
- [41] J.E. Kennedy, G.M. Roach Jr., M.F. Dowling, S.I. Abdel-Khalik, S.M. Ghiaasiaan, S. M. Jeter, Z.H. Quershi, The onset of flow instability in uniformly heated horizontal microchannels, *J. Heat Transfer* 122 (2000) 118–125.
- [42] J. Wang, Y. Huang, Y. Wang, Visualized study on specific points on demand curves and flow patterns in a single-side heated narrow rectangular channel, *Int. J. Heat Fluid Flow* 32 (2011) 982–992.
- [43] J. Lee, H. Chae, S.H. Chang, Flow instability during subcooled boiling for a downward flow at low pressure in a vertical narrow rectangular channel, *Int. J. Heat Mass Transfer* 67 (2013) 1170–1180.
- [44] M. Ledinegg, Instability of flow during natural and forced circulation, *Die Wärme* 61 (1938) 891–898.
- [45] P. Saha, M. Ishii, N. Zuber, An experimental investigation of the thermally induced flow oscillations in two-phase systems, *J. Heat Transfer* 98 (1976) 616–622.
- [46] M. Ozawa, S. Nakanishi, S. Ishigai, Y. Mizuta, H. Tarui, Flow instabilities in boiling channels: Part 1, Pressure drop oscillations, *Bull. JSME* 22 (1979) 1113–1118.
- [47] R.T. Lahey Jr., M.Z. Podowski, On the analysis of various instabilities in two-phase flow, *Multiphase Sci. Tech.* 4 (1989) 183–370.
- [48] E.P. Serov, The operation of once-through boiler in variable regimes, *Trudy, Moscow Energy. Inst.* 11 (1953).
- [49] G. Yadigaroglu, A.E. Bergles, Fundamental and higher-mode density-wave oscillations in two-phase systems, *J. Heat Transfer* 94 (1972) 189–195.
- [50] J.A. Boure, A.E. Bergles, L.S. Tong, Review of two-phase flow instability, *Nucl. Eng. Des.* 25 (1973) 165–192.
- [51] D.F. Delmastro, A. Clausse, J. Converti, The influence of gravity on the stability of boiling flows, *Nucl. Eng. Des.* 127 (1991) 129–139.
- [52] C.W. Shin, H.C. NO, Experimental study for pressure drop and flow instability of two-phase flow in the PCHE-type steam generator for SMRs, *Nucl. Eng. Des.* 318 (2017) 109–118.
- [53] L.E. O'Neill, C.R. Kharangate, I. Mudawar, Time-averaged and transient pressure drop for flow boiling with saturated inlet conditions, *Int. J. Heat Mass Transfer* 103 (2016) 133–153.
- [54] L.E. O'Neill, I. Mudawar, M.M. Hasan, H.K. Nahra, B. Ramaswamy, N.R. Hall, A. Lokey, J.R. Mackey, Experimental investigation into the impact of density wave oscillations on flow boiling system dynamic behavior and stability, *Int. J. Heat Mass Transfer* 120 (2018) 144–166.
- [55] W. Qu, I. Mudawar, Measurement and prediction of pressure drop in two-phase micro-channel heat sinks, *Int. J. Heat Mass Transfer* 46 (2003) 2737–2753.
- [56] K.H. Chang, C. Pan, Two-phase flow instability for boiling in a microchannel heat sink, *Int. J. Heat Mass Transfer* 50 (2007) 2078–2088.
- [57] H. Lee, I. Park, I. Mudawar, M.M. Hasan, Micro-channel evaporator for space applications – 1. Experimental pressure drop and heat transfer results for different orientations in earth gravity, *Int. J. Heat Mass Transfer* 77 (2014) 1213–1230.
- [58] M. Ozawa, S. Nakanishi, S. Ishigai, Y. Mizuta, H. Tarui, Flow instabilities in boiling channels: part 1, Pressure drop oscillations, *Bull. JSME* 51 (1979) 1113–1118.
- [59] V. Jovic, N. Afgan, L. Jovic, D. Spasojevic, An experimental study of the pressure drop oscillations in three parallel channel two phase flow, in: G.F. Hewitt (Ed.), *Proc. Int. Heat Transfer Conf.*, Brighton, UK, 1994, pp. 193–198.
- [60] S. Lee, V.S. Devahdhanush, I. Mudawar, Frequency analysis of pressure oscillations in large length-to-diameter two-phase micro-channel heat sinks, *Int. J. Heat Mass Transfer* 116 (2018) 273–291.
- [61] H. Yuncu, An experimental and theoretical study of density wave and pressure drop oscillations, *Heat Transfer Eng.* 11 (1990) 45–56.
- [62] W.R. Schlichting, R.T. Lahey Jr., M.Z. Podowski, An analysis of interacting instability modes, in a phase change system, *Nucl. Eng. Des.* 240 (2010) 3178–3201.
- [63] L. Tadrist, Review on two-phase flow instabilities in narrow spaces, *Int. J. Heat Fluid Flow* 28 (2007) 54–62.
- [64] S. Kakac, B. Bon, A review of two-phase flow dynamic instabilities in tube boiling systems, *Int. J. Heat Mass Transfer* 51 (2008) 399–433.
- [65] L.C. Ruspini, C.P. Marcel, A. Clausse, Two-phase flow instabilities: a review, *Int. J. Heat Mass Transfer* 71 (2014) 521–548.
- [66] J. Barber, K. Sefiane, D. Brutin, L. Tadrist, Hydrodynamics and heat transfer during flow boiling instabilities in a single microchannel, *Appl. Therm. Eng.* 29 (2009) 1299–1308.
- [67] S. Lee, I. Mudawar, Transient characteristics of flow boiling in large micro-channel heat exchangers, *Int. J. Heat Mass Transfer* 103 (2016) 186–202.
- [68] S. Lee, I. Mudawar, Thermal and thermodynamic performance, and pressure oscillations of refrigeration loop employing large micro-channel evaporators, *Int. J. Heat Mass Transfer* 103 (2016) 1313–1326.
- [69] Q. Lu, D. Chen, C. Li, X. He, Experimental investigation on flow boiling heat transfer in conventional and mini vertical channels, *Int. J. Heat Mass Transfer* 107 (2017) 225–243.
- [70] G. Xia, W. Wang, L. Cheng, D. Ma, Visualization study on the instabilities of phase-change heat transfer in a flat two-phase closed thermosyphon, *App. Therm. Eng.* 116 (2017) 392–405.
- [71] K. Miyoshi, N. Takenaka, T. Ishida, K. Sugimoto, investigation of temperature fluctuation phenomena in a stratified steam-water two-phase flow in a simulating pressurizer spray pipe of a pressurized water reactor, *Nucl. Eng. Des.* 316 (2017) 38–45.
- [72] C. Huh, J. Kim, M.H. Kim, Flow pattern transition instability during flow boiling in a single microchannel, *Int. J. Heat Mass Transfer* 50 (2007) 1049–1060.
- [73] C.A. Chen, T.F. Lin, W.-M. Yan, Time periodic saturated flow boiling heat transfer of R-134a in a narrow annular duct due to heat flux oscillation, *Int. J. Heat Mass Transfer* 106 (2017) 35–46.
- [74] I. Mudawar, Flow boiling and flow condensation in reduced gravity, *Advances in Heat Transfer* 49 (2017) 1–82.
- [75] S.M. Kim, I. Mudawar, Universal approach to predicting saturated flow boiling heat transfer in mini/micro-channels – Part II. Two-phase heat transfer coefficient, *Int. J. Heat Mass Transfer* 64 (2013) 1239–1256.
- [76] S.M. Kim, I. Mudawar, Theoretical model for local heat transfer coefficient for annular flow boiling in circular mini/micro-channels, *Int. J. Heat Mass Transfer* 73 (2014) 731–742.
- [77] S.M. Kim, I. Mudawar, Review of databases and predictive methods for heat transfer in condensing and boiling mini/micro-channel flows, *Int. J. Heat Mass Transfer* 77 (2014) 627–652.
- [78] C.R. Kharangate, L.E. O'Neill, I. Mudawar, Effects of two-phase inlet quality, mass velocity, flow orientation, and heating perimeter on flow boiling in a rectangular channel: Part 1 – Two-phase flow and heat transfer results, *Int. J. Heat Mass Transfer* 103 (2016) 1261–1279.
- [79] S.-M. Kim, I. Mudawar, Universal approach to predicting two-phase frictional pressure drop for adiabatic and condensing mini/micro-channel flows, *Int. J. Heat Mass Transfer* 55 (2012) 3246–3261.
- [80] S.M. Kim, I. Mudawar, Review of databases and predictive methods for pressure drop in adiabatic, condensing and boiling mini/micro-channel flows, *Int. J. Heat Mass Transfer* 77 (2014) 74–97.
- [81] H. Zhang, I. Mudawar, M.M. Hasan, Experimental assessment of the effects of body force, surface tension force, and inertia on flow boiling CHF, *Int. J. Heat Mass Transfer* 45 (2002) 4079–4095.
- [82] H. Zhang, I. Mudawar, M.M. Hasan, Experimental and theoretical study of orientation effects on flow boiling CHF, *Int. J. Heat Mass Transfer* 45 (2002) 4463–4478.
- [83] C. Konishi, I. Mudawar, Review of flow boiling and critical heat flux in microgravity, *Int. J. Heat Mass Transfer* 80 (2015) 469–493.
- [84] C.R. Kharangate, L.E. O'Neill, I. Mudawar, M.M. Hasan, H.K. Nahra, R. Balasubramaniam, N.R. Hall, A.M. Macner, J.R. Mackey, Effects of subcooling and two-phase inlet on flow boiling heat transfer and critical heat flux in a horizontal channel with one-sided and double-sided heating, *Int. J. Heat Mass Transfer* 91 (2015) 1187–1205.
- [85] C.R. Kharangate, L.E. O'Neill, I. Mudawar, M.M. Hasan, H.K. Nahra, R. Balasubramaniam, N.R. Hall, A.M. Macner, J.R. Mackey, Flow boiling and critical heat flux in horizontal channel with one-sided and double-sided heating, *Int. J. Heat Mass Transfer* 90 (2015) 323–338.
- [86] C.R. Kharangate, C. Konishi, I. Mudawar, Consolidated methodology to predicting flow boiling critical heat flux for inclined channels in Earth gravity and for microgravity, *Int. J. Heat Mass Transfer* 92 (2016) 467–482.
- [87] C.R. Kharangate, L.E. O'Neill, I. Mudawar, Effects of two-phase inlet quality, mass velocity, flow orientation, and heating perimeter on flow boiling in a rectangular channel: Part 2 – CHF experimental results and model, *Int. J. Heat Mass Transfer* 103 (2016) 1280–1296.
- [88] L.E. O'Neill, I. Mudawar, Mechanistic model to predict frequency and amplitude of density wave oscillations in vertical upflow boiling, *Int. J. Heat Mass Transfer* 123 (2018) 143–171.
- [89] M. Ishii, Thermally induced flow instabilities in two-phase mixtures in thermal equilibrium, Ph.D. Thesis, Georgia Institute of Technology, 1971.
- [90] L.A. Belblidia, C. Bratianu, Density-wave oscillations, *Ann. Nucl. Energy* 6 (1979) 425–444.
- [91] K. Solberg, Resultats des essais' instabilities sur la boucle 'culine' et comparaisons avec un code de calcul, C.E.N.G., Note 225, Centre d'Etudes Nucleaires de Grenoble, France, 1966.
- [92] SciPy v0.14.0 Reference Guide, Signal processing, [scipy.signal.butter](https://docs.scipy.org/doc/scipy-0.14.0/reference/generated/scipy.signal.butter.html), The scipy community (2014), accessed September 2017, <https://docs.scipy.org/doc/scipy-0.14.0/reference/generated/scipy.signal.butter.html>.
- [93] Simple real Fourier series approximation, Matt Tearle (2016), accessed September 2017, <https://www.mathworks.com/matlabcentral/fileexchange/31013-simple-real-fourier-series-approximation?focused=6790998&tab=function>.
- [94] K. Fukuda, T. Kobori, Classification of two-phase flow instability by density wave oscillation model, *J. Nucl. Sci. Technol.* 16 (1979) 95–108.
- [95] M.V.C. Alves, P.J. Waltrich, T.R. Gessner, G. Falcone, J.R. Barbosa Jr., Modeling transient churn-annular flows in a long vertical tube, *Int. J. Multiphase Flow* 89 (2017) 399–412.